STEP Team at USTC
http://space.ustc.edu.cn/dreams/

April 12, 2011, 10:54pm

Quantitative Analysis of CME Deflections in the Corona

Bin Gui[1,2], Chenglong Shen[1], Yuming Wang[1,*], Pinzhong Ye[1,2], Jiajia Liu[1], Shui Wang, and Xuepu Zhao[3]

[1] *CAS Key Laboratory of Geospace Environment Department of Geophysics & Planetary Sciences, University of Science & Technology of China, Hefei, Anhui 230026, China*

[2] *State Key Laboratory of Space Weather, Center for Space Science and Applied Research, Chinese Academy of Sciences, Beijing, China*

[3] *W.W. Hansen Experimental Physics Laboratory, Stanford University, Stanford, CA 94305, USA*

[*] *Author for correspondence, Email: ymwang@ustc.edu.cn*

Contents

Abstract. In this paper, ten CME events viewed by the STEREO twin spacecraft are analyzed to study the CME deflections during their propagation in the corona. Based on the three-dimensional information of the CMEs derived by the graduated cylindrical shell (GCS) model [Thernisien et al. 2006], it is found that the propagation directions of 8 CMEs changed. By applying the theoretical method proposed by Shen et al. [2011] to all the CMEs, we found that the deflections are consistent, in strength and direction, with the minus gradient of the magnetic energy density. There is a positive correlation between the deflection rate and the strength of the magnetic energy density gradient and a weak anti-correlation between the deflection rate and the CME speed. The preliminary results explicitly suggest that the deflections of CMEs are mainly controlled by the background magnetic field and can be quantitatively described by the magnetic energy density gradient (MEDG) model.

Keywords: Coronal Mass Ejections (CME), Deflections, Magnetic Energy Density

1 Introduction

Corona Mass ejections (CMEs) are large scale eruptions from the solar surface and act as one of the primary drivers of space weather phenomena, such as geomagnetic storm, solar energetic particle events, etc. The CME deflections, which were first reported by MacQueen et al. [1986] in Skylab epoch (1973-1974), are one of the factors influencing the geoeffectiveness of CMEs. A statistical study about CME deflections was made by Cremades and Bothmer [2004]. They identified the source regions of 124 structured CME events observed by Large Angle and Spectrometric Coronagraph (LASCO) on board the Solar and Heliospheric Observatory (SOHO) during 1996-2002 and compared the CMEs' source regions with their central position angles (CPAs). Cremades and Bothmer [2004] found that there was a systematic deflection by 20 degrees to lower latitudes at solar minimum only (1996-1998) and no systematic trend nor deflection during the years 1999-2002. The result was further confirmed by the recent work of Wang et al. [2011], in which all the LASCO CMEs during 1997-1998 were examined. In the paper by Cremades et al. [2006], a good correspondence was found between the deflection of CMEs and the total area of coronal holes (CHs). They suggested that the neighboring CHs affect the outward evolution of CMEs near the Sun and cause such deflections. Shen et al. [2011] analyzed the deflection of the 2007 October 8 CME in the meridian plane in much more details. They showed strong evidence that the trajectory of the CME was influenced by the background magnetic field, and the CME tends to deflect to the region with lower magnetic energy density.

Note that all the CME deflections studied above are in latitudinal direction. The CME deflections on a spherical surface, i.e., in both latitudinal and longitudinal directions, still remain unclear due to the presence of projection effect. Even so, the CME deflection in longitude was suggested by some researchers. For example, the longitudinal deflections of CMEs as they propagate in the interplanetary space were first proposed by Wang et al. [2004,

2006]. Such deflections can explain the east-west asymmetrical distribution of the source locations of the geoeffective halo CMEs [Wang et al., 2002]. Gopalswamy et al. [2004, 2005, and 2009] also suggested that CMEs could be deflected away from the Sun-Earth line by the associated coronal holes. They use such deflections to explain the existence of the 'driverless' shocks, which were observed near the Earth but without their drivers, the interplanetary coronal mass ejections (ICME).

Since the successful launch of the Solar TErrestrial RElations Observatory (STEREO) mission [Kaiser et al., 2008], the three-dimensional (3-D) information of CMEs is more or less revealed in observations with the aid of various reconstruction models [e.g., Thernisien et al. 2006, 2009; Lugaz et al., 2010; Liu et al., 2010a, b]. STEREO consists of two identical satellites. It for the first time provided the observations of the Sun from dual vantage points. Based on the STEREO observations, some CME events with an obvious deflection in the latitudinal direction have been reported [e.g. Kilpua et al., 2009; Shen et al., 2011], and the possible deflections of CMEs in the ecliptic plane have also been discussed [e. g., Liu et al, 2010b; Lugaz et al. 2010; Poomvises et al., 2010].

In this paper, we have comprehensively studied the CME deflections in the corona in both latitudinal and longitudinal directions for ten CME events viewed by the STEREO twin spacecraft. The data and the method we used are introduced in the next section. In Section 3, four cases are selected to show different types of deflections, in which their 3-D trajectories and the comparisons between the deflections and the magnetic energy density distributions are presented. In Section 4, preliminarily statistical results of the deflection and its correlation with the magnetic energy density are obtained. Finally, we give the conclusions and make some discussions in Section 5.

2 Data and Method

2.1 Three-dimensional information of CMEs

The observations from the COR1 and the COR2 instruments of the Sun Earth Connection Coronal and Heliospheric Investigation (SECCHI) [Howard et al., 2008] suite on board the STEREO A and B spacecraft are used to learn about the evolutions of CMEs in the corona. The COR1 instruments observe the corona from 1.4-4.0 R_s and the COR2 instruments observe the corona from 2.5-15.0 R_s. In this paper, these observations were used to obtain the 3-dimensional information of CME during its propagation in the corona. The observations from the SECCHI/EUVI and the Michelson Doppler Imager (MDI) on board SOHO [Brueckner et al., 1995] are used to identify the CMEs' source regions on the solar surface.

To obtain the 3-D geometry and therefore the trajectory of a CME, the Graduated Cylindrical Shell (GCS) model developed by Thernisien et al. [2006, 2009] was applied to both the projected two-dimensional images from the STEREO-A (STA) and the STEREO-B (STB). In that model, CMEs are assumed to have a flux rope-like structure. The GCS model has nine free parameters (refer to Table 1 of Thernisien et al. 2006). Six of them determine the CME's shape projected on the plane-of-sky. These parameters, referred to as geometric parameters, are the longitude 'ϕ' and latitude 'θ', height 'h' (the height of the legs, or 'h_f', the height of the leading edge), aspect ratio 'κ', tilt angle 'γ' with respect to the equator, and half angular width 'α' between the flux rope legs. The other three parameters, deciding the electron density distribution at the shell, are the electron density factor 'N_ε', Gaussian width '$\sigma_{trailing}$' of the density profile in the interior of the GCS and Gaussian width '$\sigma_{leading}$' of the density profile at the exterior of the GCS.

A set of reasonable initial values of the parameters is helpful to get the best fitting of the CME images. Observations of the CME source region on the solar surface were used to constrain the initial values of longitude ϕ, latitude θ and tilt angle γ if any. The tilt angle can be estimated according to the CME-associated filament (or the polarity inversion line, PIL, if no filament observed) because it is believed that a CME is a flux rope surrounding its associated filament and standing above the PIL. The rest of the parameters are set by comparing the GCS flux rope to the CME shape observed simultaneously by both the STA and the STB. In practice, we find that the tilt angle and half angle are insensitive to the fitting results. Therefore we fix them to a certain reasonable value for the whole CME evolution process by trial and error. It should be noted that fixing the tilt angle indicates a CME without rotation, which may not be true for many CME events [Lynch et al., 2009; Möestl et al., 2008; Shiota et al., 2010, Török and Kliem, 2003; Wang et al. 2006; Yurchyshyn et al., 2007, 2009]. However, we find that the change of the tilt angle

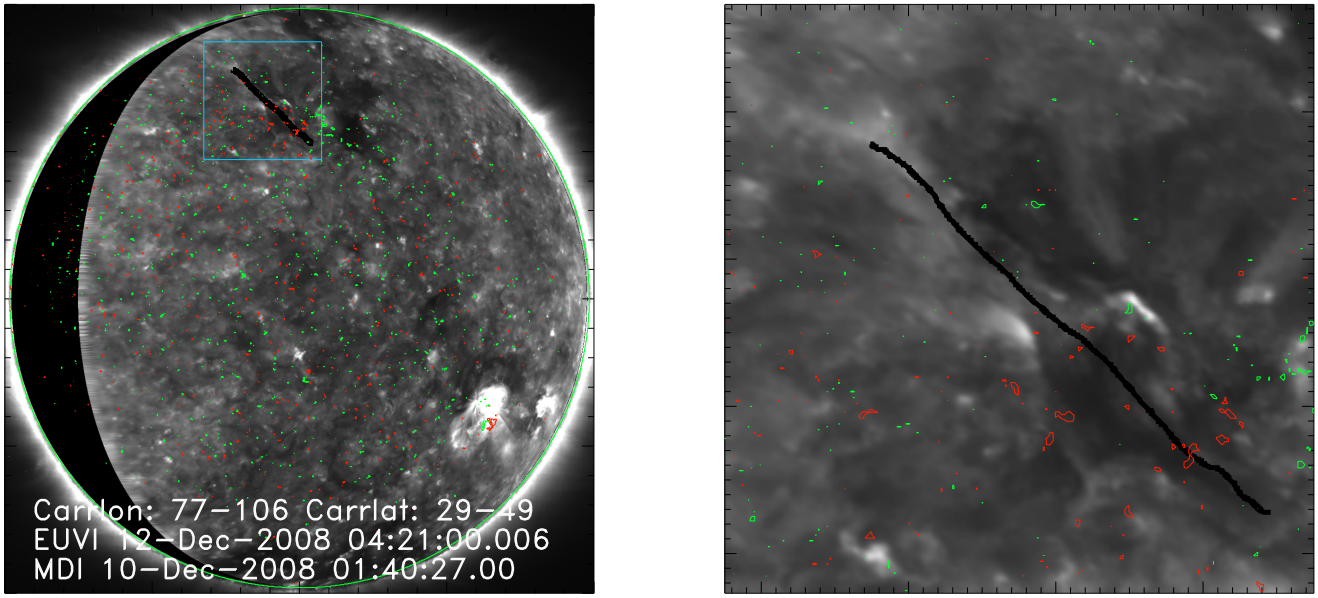

Figure 1: The source region of the 2008 December 12 CME observed by the STEREO/EUVI and the SOHO/MDI. Panel (a) shows the STEREO/EUVI 171 Å image superposed by the contours of the SOHO/MDI magnetogram taken two days ago when the source region (marked by the square box) was visible to the SOHO. The STEREO/EUVI image was rotated to match the angle of view of the SOHO/MDI. Panel (b) shows the zoomed-in image of the source region.

will not significantly affect the derived directions of CMEs as long as the GCS flux rope matches the observed CME shape in both the STA and STB images (see the discussion in Sec.5). Thus, in this study a fixed tilt angle is acceptable. Besides, not all the CMEs in our sample have available observations of their source regions. For such events, we just compare the GCS flux rope with observed CME shape to get the parameters.

2.2 Coronal magnetic filed

It is believed that the magnetic energy is dominant in the corona. Previous studies have suggested that the CME deflection can be qualitatively interpreted as the constraint of the ambient magnetic structure, e.g., coronal holes [Gopalswamy et al., 2004]. Our recent study of the 2007 October 8 CME showed that the behavior of the CME's latitudinal deflection can be quantitatively described by a theoretical method, in which the magnitude of the deflection is well consistent with the minus gradient of magnetic energy density, $< -\nabla(\frac{B^2}{2\mu_0}) >$, where the angle brackets mean the average over the region occupied by the CME [Shen, et al., 2011]. In that work, however, the deflection in the latitudinal direction of only one CME was studied. Thus, we test the method with more CME events to check if it is also applicable to other CMEs and to the deflections in other directions.

In the method, the 3-D magnetic field of the corona is key information, and is extrapolated from the SOHO/MDI photospheric magnetic synoptic charts by the Current Sheet-Source Surface (CSSS) model developed by Zhao et al. [1995]. The CSSS model is a development of the PFSS model, and was used in our previous work [e.g., Shen, et al., 2007, 2011; Wang & Zhang, 2007]. The magnetic synoptic chart is created from the MDI daily magnetograms over a quasi-27-day solar rotation. It can not reflect the state of the photosphere right at the time of a CME taking place. However, what we are interested in is the large scale coronal magnetic field, which probably changes little during a solar rotation [Ness & Wilcox, 1964]. Under this consideration, the synoptic chart may be treated as a good approximation to the real photospheric magnetogram over the full solar surface. In this study, the magnetic synoptic charts with spatial resolution of $360^o \times 180^o$ are used. To get the best extrapolation results, the order of the harmonic coefficients is chosen 125. Once the coronal magnetic field is extrapolated, the average gradient of the magnetic energy density can be easily calculated for any CMEs of interest.

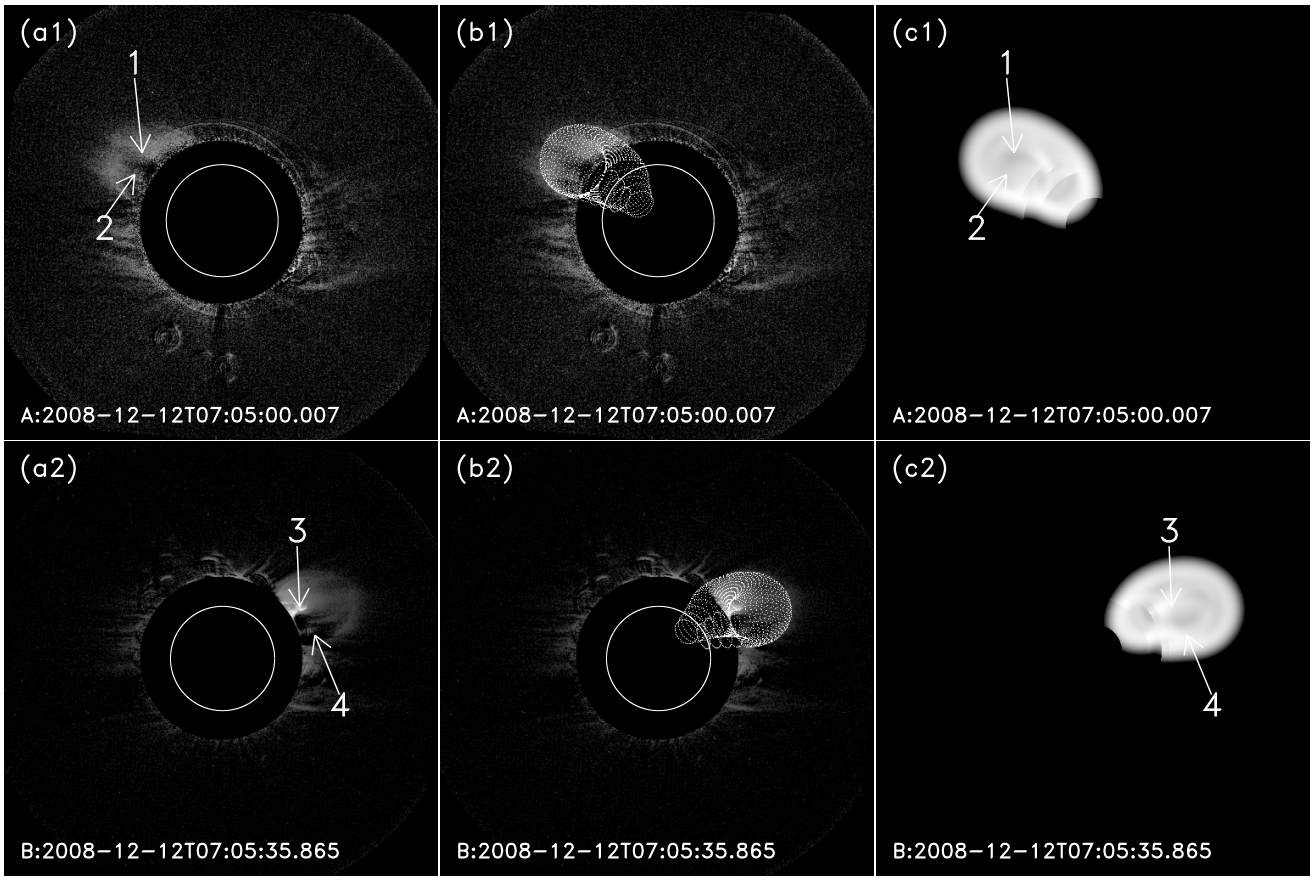

Figure 2: The fitting example of CME-1. From (a) to (c): The original CME images, the modeled wireframe images which overlay on the CME images and the relative brightness derived from the GCS model. The upper and bottom panels present the results based on the STA and the STB, respectively. The arrows with numbers indicate the common points of the CME between the original images and the derived brightness images.

3 Observations and model analyses of four cases

Before we show the statistical results of ten CMEs, in this section four different types of CMEs are selected to detailedly present the deflection behaviors and their relationship with the gradient of the coronal magnetic energy density. The first case is the 2008 December 12 event (CME-1), which deflected in the latitudinal direction. The second case is the 2008 April 9 event (CME-2), which deflected in the longitudinal direction. The third case is a CME erupting on 2007 November 16 (CME-3), in which a deflection in both latitudinal and longitudinal directions are obvious. The last case is the 2008 November 3 event (CME-4), which did not show an evident deflection.

3.1 The 2008 December 12 event (CME-1)

This CME first appeared in the field of view (FOV) of the STA/COR1 and the STB/COR1 at about 05:35 UT on 2008 December12. To fit the CME with the GCS model, it is required that the CME almost fully appeared in the FOV of the coronagraph. Thus the first and the last COR1 image pairs we selected are taken at 05:35 UT and 07:35 UT, respectively, during which there are 13 image pairs (or data points) with a cadence of 10 minutes. Similarly, in COR2 FOV, the first and last image pairs are taken at 09:52 UT and 14:52 UT, respectively, and there are 11 image pairs with a cadence of 30 minutes.

This CME was associated with a filament, which erupted at about 04:00 UT on 2008 December 12. The square area in Figure 1(a) represents the source region of the CME by combining the STEREO_A/EUVI and SOHO/MDI observations. The MDI magnetogram is contoured on the map of the EUVI 171 Å image as indicated by the red (positive) and green (negative) lines, and the EUVI image is rotated to match the time and the vantage point of the MDI data. The black curve in

the square displays the filament. This filament extended over a long and narrow region, from about 77° to 106° in longitude and about 29° to 49° in latitude under the Carrington Coordinate system.

Figure 1(b) shows the zoomed-in image of the CME source region. As have been mentioned in the last section, the tilt angle and the half angle are fixed to a certain value for the whole evolution process of the CME. After applying a trial and error method, we find that, with the value of −15° for tilt angle and 14° for half angle, the GCS model can reach the best fitting result in visual.

Time/UT	ϕ_c/°	ϕ_s/°	θ/°	h_f/R_s	κ
		COR1			
05:35	72.8	2.0	30.7	2.46	0.22
05:45	73.6	2.9	29.3	2.52	0.23
05:55	73.8	3.2	28.1	2.59	0.23
06:05	72.2	1.7	28.0	2.66	0.23
06:15	74.8	4.4	27.7	2.76	0.23
06:25	74.5	4.1	26.6	2.81	0.24
06:35	74.2	4.0	26.5	2.89	0.24
06:45	75.1	4.9	25.5	2.98	0.24
06:55	77.5	7.4	22.9	3.24	0.26
07:05	78.7	8.7	22.9	3.29	0.26
07:15	75.7	5.8	22.6	3.50	0.27
07:25	76.8	7.0	20.8	3.67	0.28
07:35	76.6	6.9	19.2	3.81	0.28
		COR2			
09:52	76.4	8.0	12.2	7.25	0.29
10:22	76.2	8.0	11.7	7.92	0.29
10:52	74.9	7.0	11.7	9.17	0.29
11:22	75.6	8.0	11.5	9.93	0.29
11:52	73.3	6.0	10.9	11.13	0.29
12:22	74.7	7.6	10.7	11.68	0.29
12:52	74.9	8.1	9.8	13.02	0.29
13:22	77.2	10.7	9.5	14.12	0.29
13:52	75.0	8.7	9.5	14.70	0.29
14:22	75.3	9.3	9.6	16.26	0.29
14:52	74.3	8.6	9.6	17.36	0.29

Table 1: The fitted free parameters of the 2008 December 12 CME derived by the GCS model with the tilt angle of −15° and the half angle of 14°

Further, we fit the observed CME shape with the GCS model for each image pair. Figure 2 shows the sample of the fitting result of the CME recorded at 07:05 UT. Figure 2(b1) and (b2) present the wireframe of the GCS flux rope which overlaid to the original images. From these two images, we found that the shapes of the CME are both consistent with the wireframe. Figure 2(c1) and (c2) present the relative brightness images derived from the GCS model. By comparing the Figure 2c with 2a, we find that they are quite similar. The arrows marked in these sub-figures denote some common points: the bright features in Figure 2(a) are also bright in Figure 2(c) (arrow 1 and 3), and the darker features in Figure 2(a) also look darker in Figure 2(c) (arrow 2 and 4). These results indicate that the GCS model not only fits the projected shape of the CME well, but also could reflect the relative brightness of the CME. Based on the above analysis, we are quite confident that the derived parameters should well reflect the 3-D geometry of the CME.

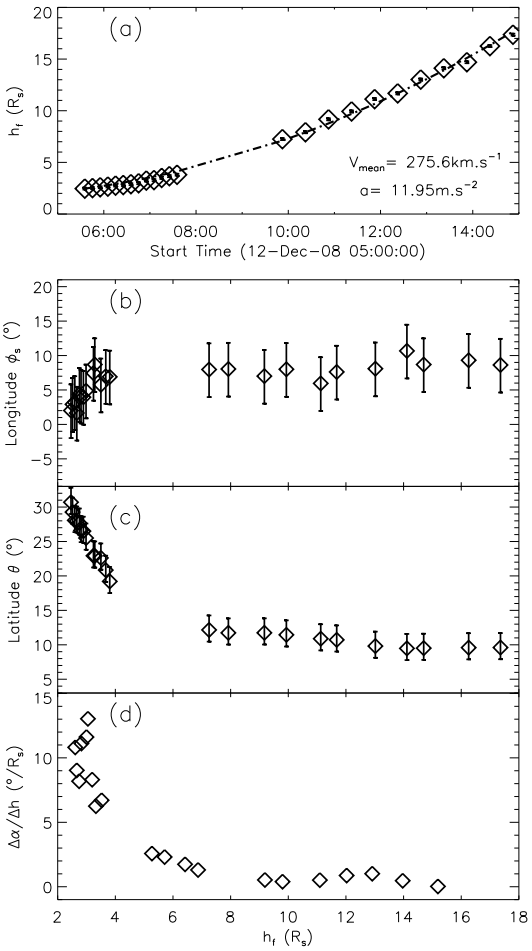

Figure 3: The kinetic evolution of the CME-1 event. Panels (a) to (d) show the height-time, Stonyhurst longitude-height, latitude-height, and deflection rate-height plots, respectively. The error bars in the first three panels are got from the 10% decrease of the merit function [see Thernisien et al., 2009 for details]

After all the 24 image pairs are processed, the CME trajectory is obtained. All the fitted free parameters are listed in Table 1. The first column gives the time when the CME was recorded by the STEREO/SECCHI instrument. The next two columns give the longitude under the Carrington coordinate system ('ϕ_c') and the Stonyhurst coordi-

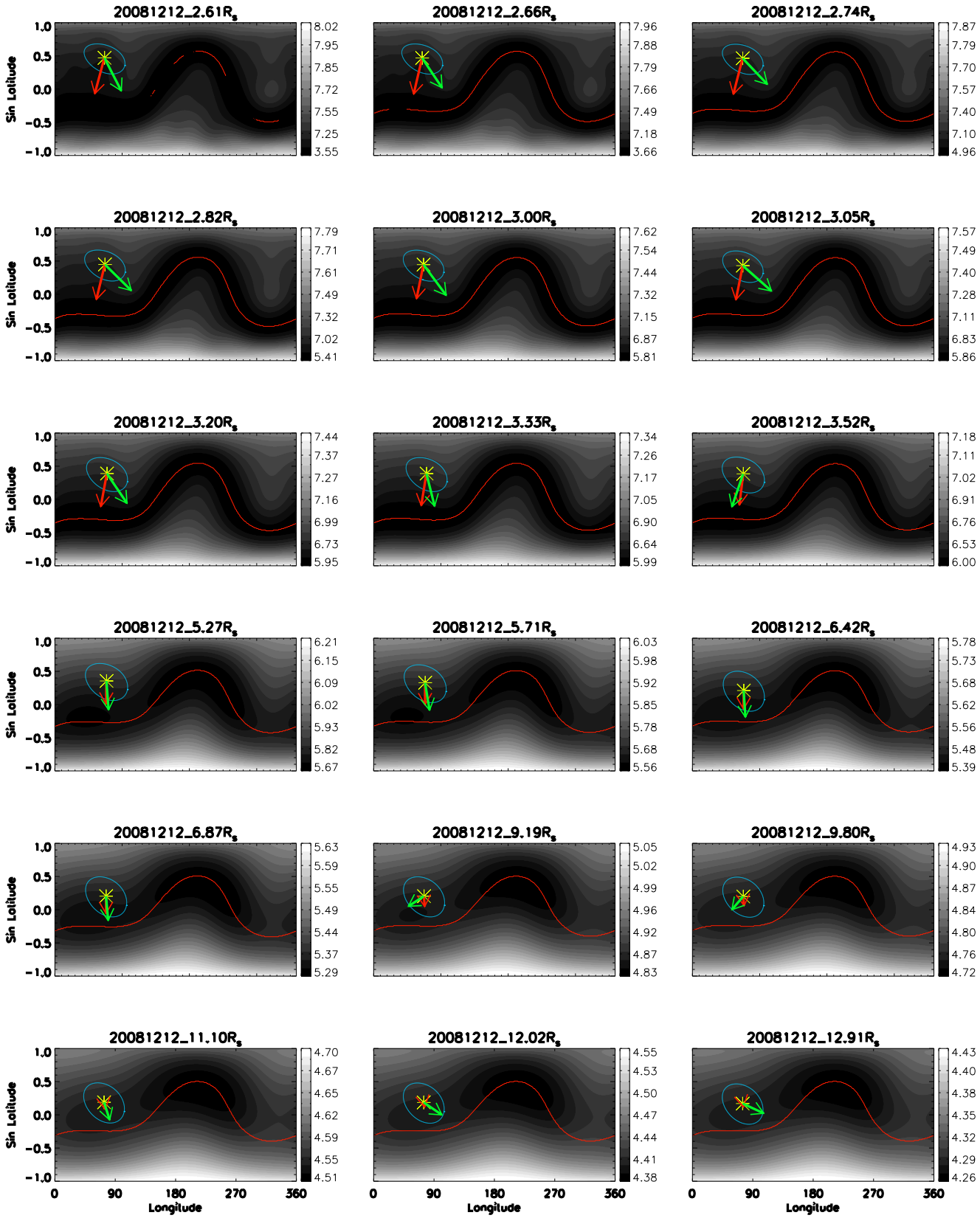

Figure 4: The comparison between the minus gradient of the magnetic energy density and the CME-1's deflection. The magnetic field energy density contour in each panel is calculated based on the extrapolated coronal magnetic field at the corresponding altitude. The unit of the color bar of the contour is J.km$^-$3 in logarithm. The Leading edge projection on the Carrington map is indicated by the yellow asterisk. The deflection and the minus gradient are presented by the green and red arrows, respectively. The lengths of the green and red arrows indicate the deflection rate and the relative strength of the minus gradient, respectively. The red curves indicate the heliospheric current sheet, which appears above about 2.6 R_s where all the coronal magnetic field lines open.

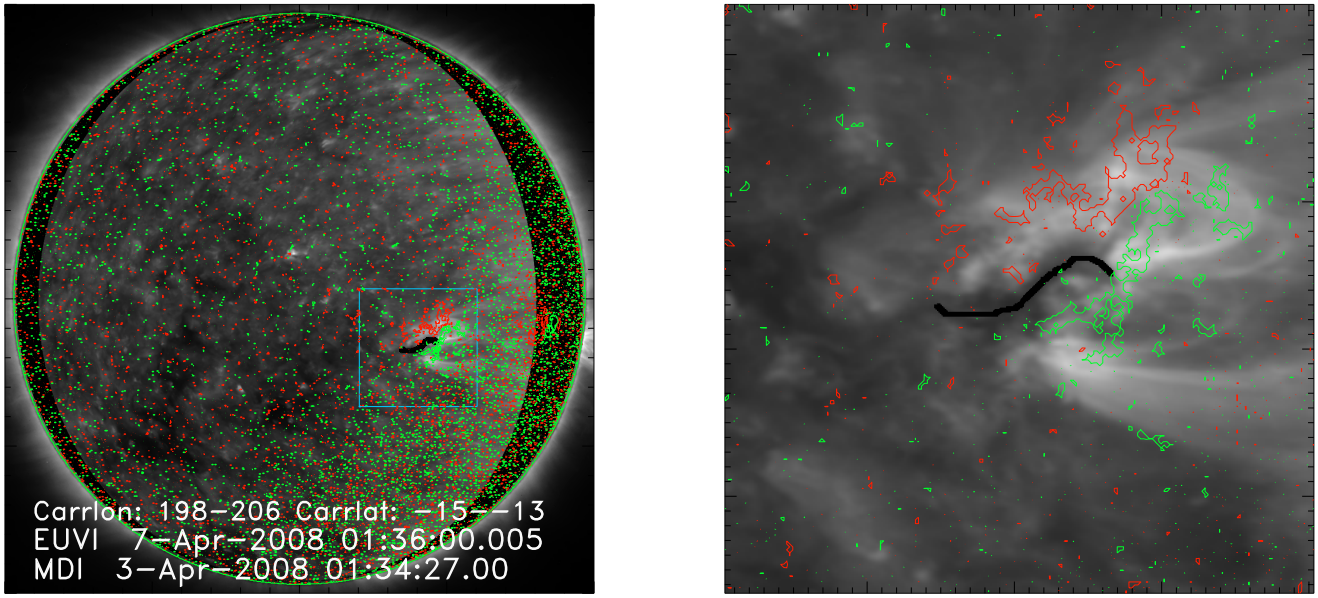

Figure 5: The source region of the 2008 April 9 CME observed by the STEREO/EUVI and the SOHO/MDI. Panel (a) shows the STEREO/EUVI 171 Å image superposed by the contours of the SOHO/MDI magnetogram taken at two days ago when the source region (marked by the square box) was visible to the SOHO. The STEREO/EUVI image was rotated to match the angle of view of the SOHO/MDI. Panel (b) shows the zoomed-in image of the source region.

nate system ('ϕ_s') [Thompson, 2006], respectively. The next three columns give the other geometric parameters: latitude 'θ', height 'h_f', ratio 'κ'.

Figure 3(a) shows the height-time plot of the CME. Both linear and quadratic fittings are applied to the measurements. It is found that this CME was propagating outward with a speed of about $275.6km \cdot s^{-1}$ and an acceleration of about $12m \cdot s^{-2}$. Figure 3(b) and 3(c) present the Stonyhurst longitude and latitude as a function of the height, respectively. The Stonyhurst longitude changed around the value of 5° with $\sim$ 4° variation. Considering the error in our fitting process, this CME did not manifest an evident deflection in the longitude. But its latitude shows a clear variation from about 30° to 10°, which suggests that the CME experienced an evident deflection from high latitude to low latitude.

Further, we define the deflection rate as $\triangle\alpha/\triangle h$, where $\triangle\alpha$ is the deflection angle (both latitudinal and longitudinal deflection are taken into account). For events with more than 10 data points, the deflection rate at any data point is calculated by fitting the longitude and the latitude with height of neighboring five data points. For events with less than 10 data points, a fitting procedure over 3 neighboring data points is used. The variation of the deflection rate with the height is shown in Figure 3(d). It is clear that the deflection rate decreases quickly as the height increases. The main deflection of the CME occurred in the range below about 8 R_s. When the CME's leading edge exceeded 8 R_s, the deflection became insignificant. This event has been previously studied by some other researchers [e.g., Byrne et al., 2010; Davis et al., 2009; Liu et al., 2010b, Poomvises et al. 2010, Lugaz et al., 2010]. The results we obtained here are consistent with their results.

On the other hand, the magnetic field energy density distribution at corresponding altitude for every data points is calculated. The SOHO/MDI magnetic synoptic chart of the 2077 Carrington rotation which begins at 07:00 UT 2008 November 20 and ends at 14:38 UT 2008 December 17 is used as the bottom boundary for the CSSS model. Figure 4 shows the distributions of the magnetic energy density at different altitudes. The red curves indicate the position of the heliospheric current sheet (HCS, only marked in the panels with the altitude is larger than 2.6 Rs, where the coronal magnetic field is open). The yellow asterisk marks the projected location of the CME leading edge on the Carrington map, and the cyan ellipse indicates the boundary of the CME projection. The average value of the minus gradient of the magnetic energy density in the ellipse is marked by the red arrow, and the cor-

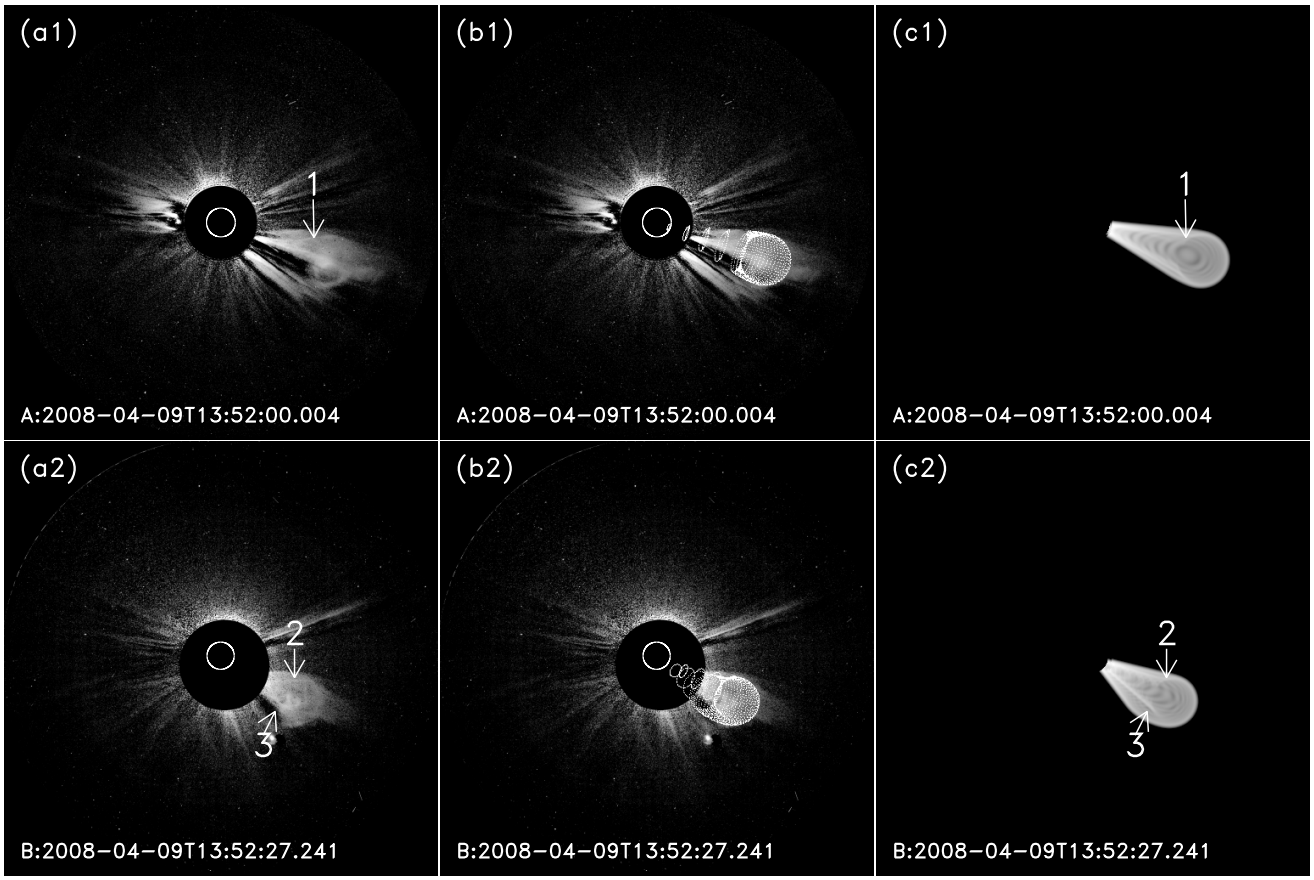

Figure 6: The fitting example of the CME-2. From (a) to (c): The original CME images, the modeled wireframe images which overlays on the CME images and the relative brightness derived from the GCS model. The upper and bottom panels present the results based on the STA and the STB, respectively. The arrows with numbers indicate the common points of the CME between the original images and the derived brightness images.

responding CME deflection is marked by the green arrow. The length of the arrows indicates the relative strength of the minus gradient and the deflection rate. The length is scaled by comparing its strength with all the data points of the ten CMEs. From the figure, it can be seen that the CME deflection is consistent well with the minus gradient of the magnetic energy density in both strength and direction, which roughly points from high latitude to low latitude. As a consequence, the CME leading edge was getting closer to the HCS during its propagation.

3.2 The 2008 April 9 CMEs (CME-2)

This CME first appeared in the FOVs of the STA/COR1 and STB/COR1 at about 10:45 UT on 9 April 2008. To guarantee the CME almost fully appeared in the FOV, the first and last image pairs of COR1 data was taken at 10:45 UT and 11:25 UT, respectively. There are 5 image pairs during the interval. The first and last images of COR2 data are taken at 13:22 UT and 14:52 UT, respectively, and a total of 4 image pairs are selected.

The CME was associated with an eruptive filament which erupted at about 09:21 UT on 9 April 2008 seen from the STB. Figure 5(a) represents the combined image of the STEREO_A/EUVI 171 Å data and the SOHO/MDI data. The square box denotes the source region of the CME. The filament marked by the black line located from about 198° to 206° in Carrington longitude and about −13° to −15° in latitude. Figure 5(b) shows the detailed image of the source region.

Similar to the fitting procedure applied to the CME-1, we fix the tilt angle and half angle to 8° and 11°, respectively, by trial and error. Then we fit the CME shapes for each image pair with the GCS model. Figure 6 shows the sample of the fitting result of the CME which recorded at 13:52 UT. The wireframe of the model matches well with the CME shapes viewed in both the STA and the

Time/UT	ϕ_c/°	ϕ_s/°	θ/°	h_f/R_s	κ
		COR1			
10:45	187.6	96.6	-21.9	2.29	0.22
10:55	190.1	99.2	-21.2	2.53	0.22
11:05	192.5	101.7	-21.1	2.75	0.22
11:15	193.5	102.9	-20.1	3.03	0.22
11:25	193.3	102.8	-19.3	3.30	0.22
		COR2			
13:22	197.8	108.2	-18.6	8.50	0.22
13:52	198.8	109.5	-18.9	9.85	0.22
14:22	201.3	112.3	-19.1	11.46	0.22
14:52	201.6	112.9	-18.6	12.70	0.22

Table 2: The fitted free parameters of the 2008 December 12 CME derived by the GCS model with the tilt angle of 8° and the half angle of 11°

STB (Fig. 6(a) and 6(b)). Figure 6(c1) and 6(c2) present the relative brightness of the CME derived from the GCS model. They are quite similar with the observed bright structure in Figure 6(a1) and 6(a2). The arrows in the figure mark some example common points between the modeled relative brightness images and the observed images. Thus, we believe that the 3-D geometry of the CME is reproduced by the GCS model. Table 2 lists the other parameters derived by the model with the tilt angle of 8° and the half angle of 11° of all the 9 image pairs of the CME.

Figure 7(a) shows the height-time plot of the CME. The average speed of the CME is 476.3 $km \cdot s^{-1}$, and the average acceleration is 20 $m \cdot s^{-2}$. The variations of the Stonyhurst longitude and latitude of the CME are shown in Figure 7(b) and 7(c). Different from the CME-1, this CME manifested a weak deflection in longitudinal direction, but no obvious deflection in latitudinal direction. Its longitude systematically changed by about 16° from $\sim 97°$ to $\sim 113°$ though the errors are large. The deflection rate of the CME is presented in Figure 7(d). For the CME-2, the fitting of the longitude and latitude with height over 3 neighboring data points is used to calculated the deflection rate as there are just nine data points in total. Similar to the CME-1, the deflection mainly occurred at the low altitude where the deflection rate is as large as $\sim 10°/R_s$, and it quickly decreased to about $1°/R_s$ beyond $\sim 3-5R_s$.

The deflections of every data points and the magnetic field energy density distributions of the CME-2 are compared as shown in Figure 8. The synoptic chart of the 2068 Carrington rotation, which begins at 01:18 UT 2008 March 20 and ends at 08:09 UT

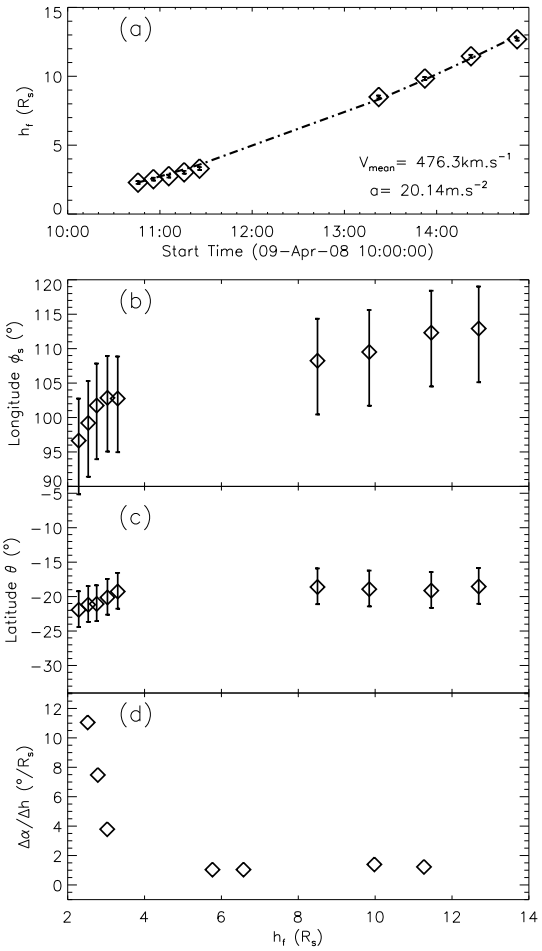

Figure 7: The kinetic evolution of the CME-2 event. Panels (a) to (d) show the height-time, Stonyhurst longitude-height, latitude-height, and deflection rate-height plots, respectively. The error bars in the first three panels are got from the 10% decrease of the merit function [see Thernisien et al., 2009 for details]

2008 April 16 is used as the bottom boundary of the CSSS model. From the figure, it can be seen that the minus gradient direction of the magnetic energy density is mainly aligned to the deflection at the low altitude. While at the higher altitude, the angle between the two arrows becomes bigger. However, the gradient of the magnetic energy density and the deflection rate both decreased to quite low levels at the high altitude. Same as the CME-1, the CME leading edge also get close to the HCS during the propagation.

3.3 The 2007 November 16 CMEs (CME-3)

The CME-3 first appeared in the COR1 FOV at about 07:35 UT on 16 November 2007. The first and last image pairs of the COR1 data were selected at 09:35 UT and 10:35 UT, respectively.

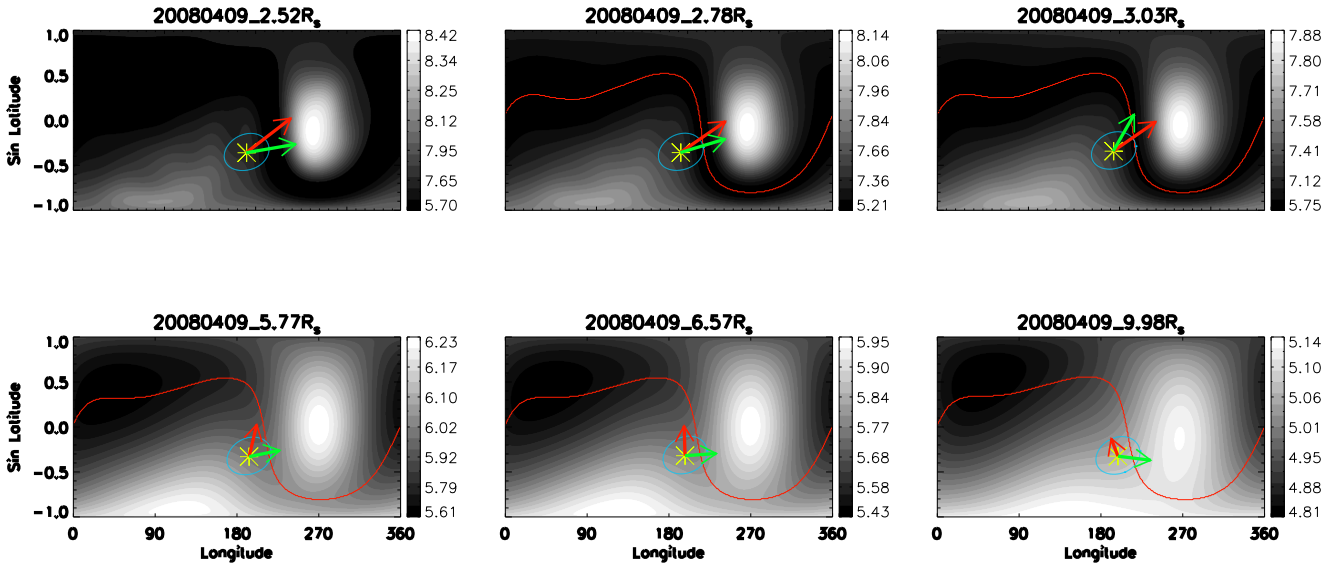

Figure 8: Same as the Figure 4, but for the 2008 April 9 CME.

During the interval, there are 7 data points. The first and the last images of the COR2 data are taken at 13:52 UT and 15:22 UT, respectively, and a total of 4 data points are selected.

Although the CME-3 erupted from the front side of the solar surface, there is no significant surface activity could be found. So, all the parameters are obtained by the image fitting. For this event, the optimized tilt angle and half angle are -25^{o} and 8^{o}, respectively, when the GCS model can reach the best fitting of the CME images. As shown in the Figure 9, the GCS flux rope can fit the CME fairly well. Table 3 lists the parameters of the event.

Time/UT	$\phi_c/^{o}$	$\phi_s/^{o}$	$\theta/^{o}$	h_f/R_s	κ
		COR1			
09:35	303.1	101.1	-22.2	3.04	0.25
09:45	306.9	105.0	-22.1	3.21	0.25
09:55	310.2	108.3	-21.6	3.29	0.25
10:05	310.7	108.9	-21.2	3.36	0.26
10:15	311.6	110.0	-21.2	3.43	0.26
10:25	312.8	111.3	-21.0	3.56	0.26
10:35	314.2	112.7	-20.0	3.71	0.26
		COR2			
13:52	318.1	118.5	-14.3	8.71	0.26
14:22	321.8	122.4	-14.7	9.73	0.27
14:52	322.9	123.8	-14.2	10.93	0.27
15:22	322.4	123.6	-13.6	11.97	0.27

Table 3: The fitted free parameters of the 2007 November 16 CME derived by the GCS model with the tilt angle of -25^{o} and the half angle of 8^{o}

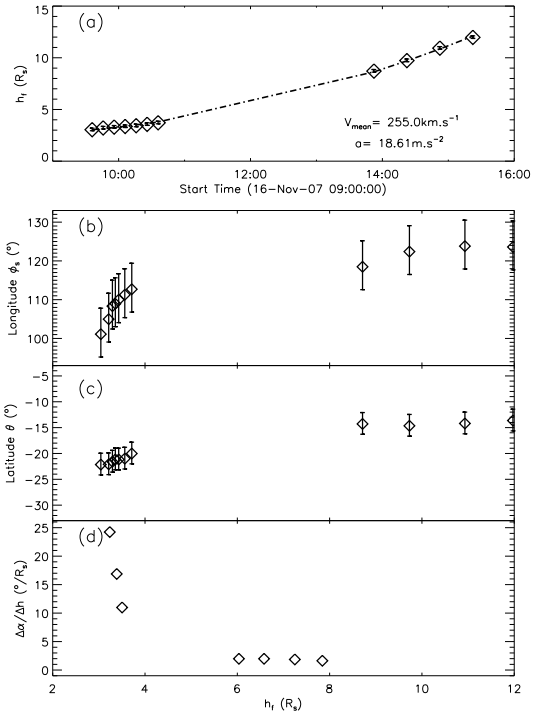

Figure 10: The kinetic evolution of the 2007 November 16 event.

Figure 10(a) shows the height-time plot of the CME. The average speed of the CME is $255.0km \cdot s^{-1}$, and the average acceleration is $19m \cdot s^{-2}$. The variations of the Stonyhurst longitude and latitude of the CME are shown in Figure 10(b) and 10(c). Different from the above two events, the CME manifested an evident deflection in both longitude and

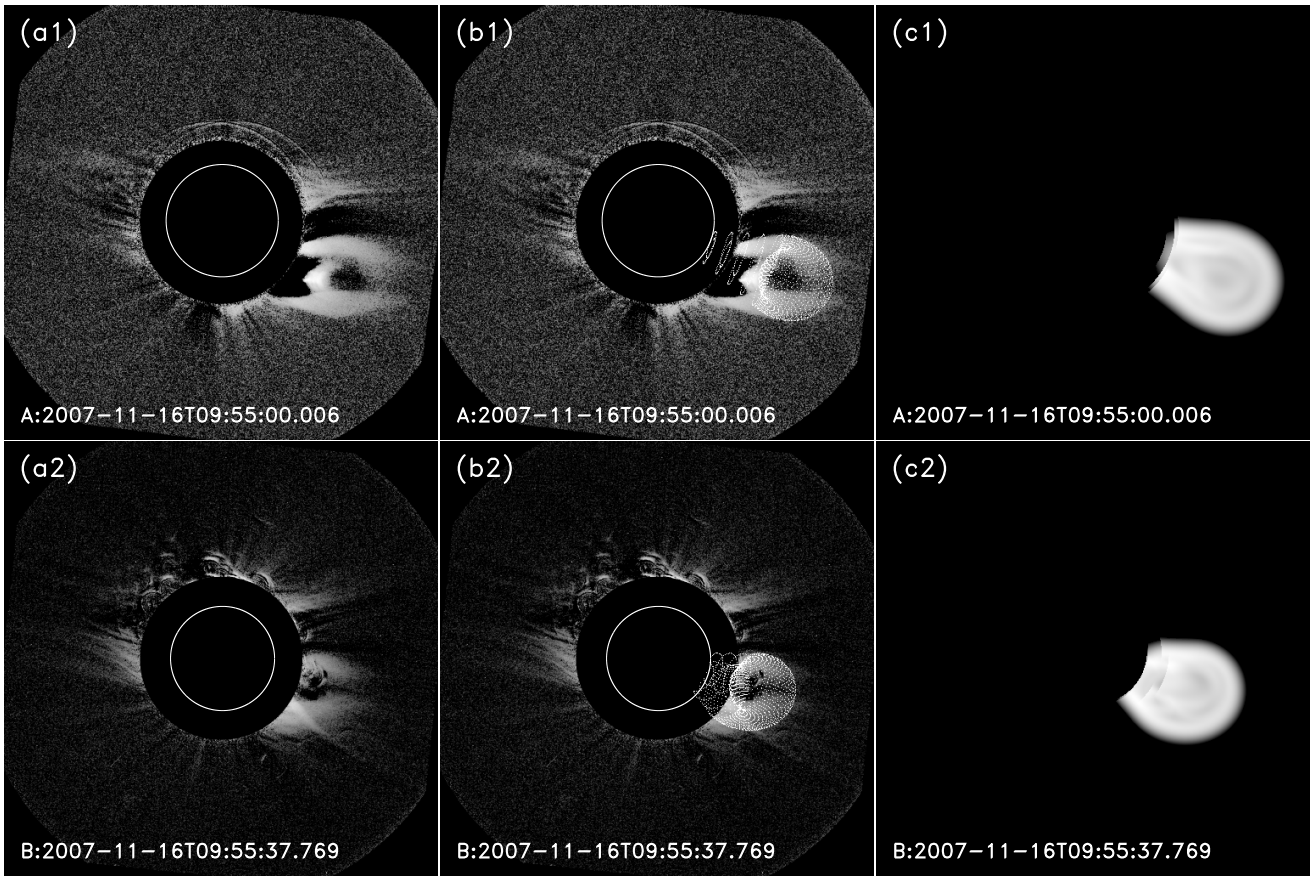

Figure 9: The fitting example of the CME-3. From (a) to (c): The original CME images, the modeled wireframe images which overlays on the CME images and the relative brightness derived from the GCS model. The upper and bottom panels present the results based on the STA and the STB, respectively.

latitude. The Stonyhurst longitude systematically changed from $\sim -101^{\rm o}$ to $\sim 124^{\rm o}$ while the latitude systematically changed from $\sim -22^{\rm o}$ to $\sim -14^{\rm o}$. The deflection rate is presented in Figure 10(d). It is found that the event has higher deflection rate at the lower altitudes, and the deflected rate quickly decreased to about $1^{\rm o}/R_s$ beyond $\sim 6R_s$.

The deflections and the magnetic field energy density distributions of every data points of the CME-3 are compared as shown in Figure 11. The synoptic chart of the 2063 Carrington rotation, which begins at 10:03 UT 2007 November 4 and ends at 17:29 UT 2007 December 1 is used. From this figure, it is found that the minus gradients of the magnetic energy density are well aligned to the deflections. The previous two CMEs occurred far away from the HCS, and then deflected towards the HCS. However, this CME almost initially originated near the HCS, and deflected along the HCS.

Time/UT	$\phi_c/^{\rm o}$	$\phi_s/^{\rm o}$	$\theta/^{\rm o}$	h_f/R_s	κ
		COR1			
00:05	235.5	7.6	22.6	3.22	0.23
00:15	235.5	7.7	21.8	3.36	0.23
00:25	234.6	6.9	21.3	3.61	0.23
00:35	236.6	9.0	21.2	3.80	0.23
00:45	236.5	8.9	21.6	3.93	0.23
00:55	235.9	8.5	20.5	4.27	0.23
01:05	236.8	9.5	19.6	4.57	0.23
		COR2			
03:22	236.9	10.8	18.2	7.51	0.23
03:52	236.1	10.3	18.4	8.50	0.23
04:22	235.5	9.9	18.4	9.41	0.23
04:52	236.4	11.2	18.1	10.14	0.23
05:22	235.5	10.5	18.5	10.95	0.23
05:52	235.2	10.5	18.6	11.97	0.23
06:22	233.6	9.2	19.0	12.64	0.23
06:52	234.6	10.4	19.0	13.09	0.23

Table 4: The fitted free parameters of the 2008 November 3 CME derived by the GCS model with the tilt angle of $-10^{\rm o}$ and the half angle of $11^{\rm o}$

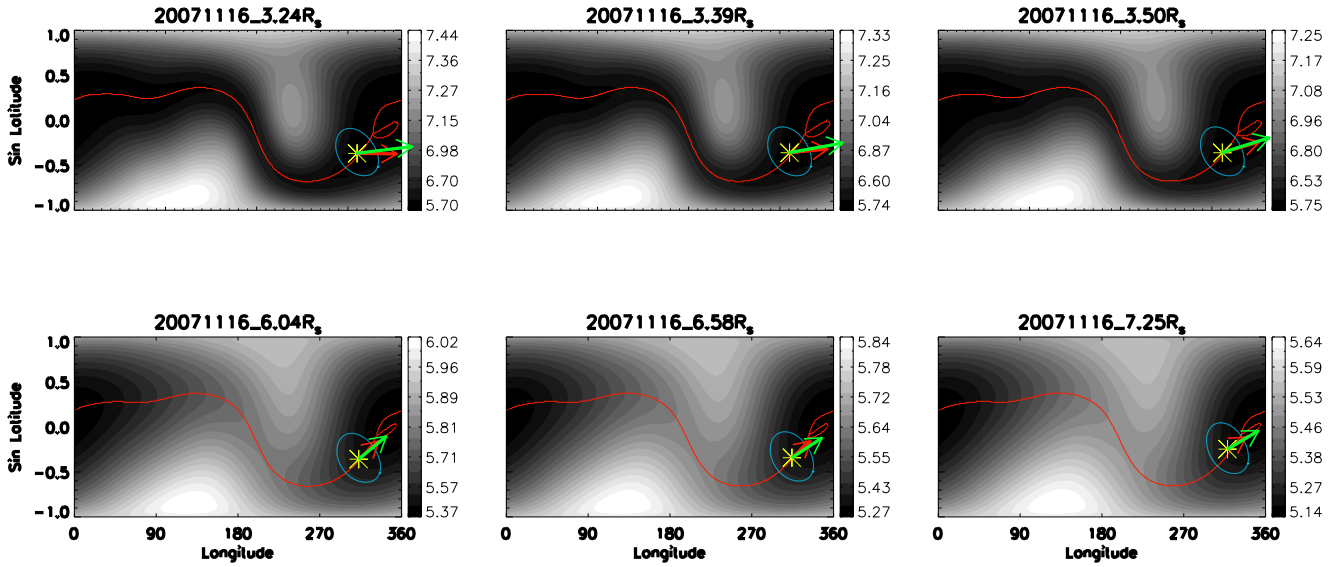

Figure 11: Same as the Figure 4, but for the 2007 November 16 event.

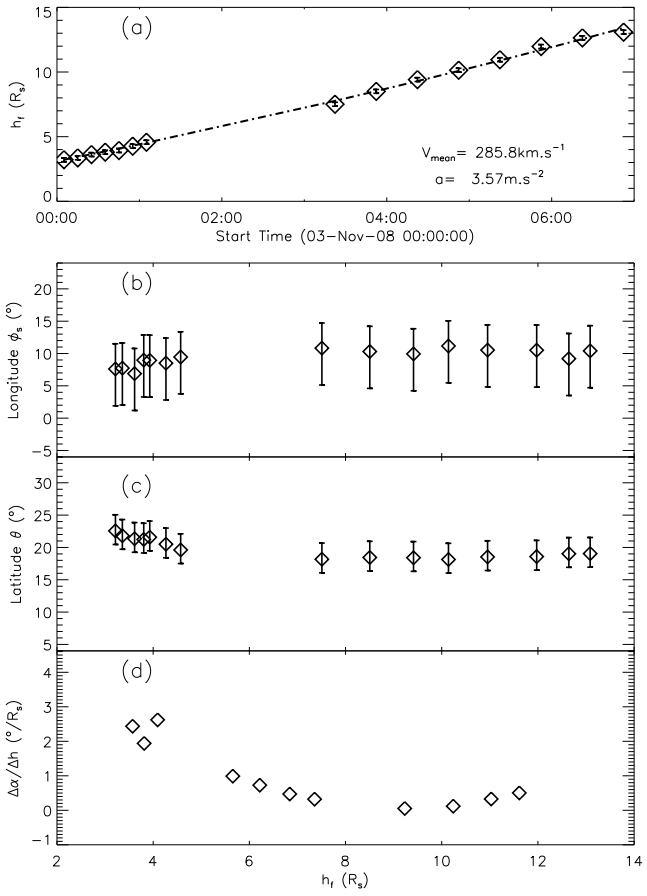

Figure 13: The kinetic evolution of the 2008 November 3 event.

3.4 The 2008 November 3 CME (CME-4)

This CME first appeared in the COR1 FOV at about 23:35 UT on 2 November 2008. The first and last images of the COR1 data were taken at 00:05 UT and 01:05 UT on 3 November 2008, respectively, and there are 7 image pairs during the interval. The first and last images of the COR2 data are taken at 03:22 UT and 06:52 UT, respectively, and a total of 8 data points are selected.

Same as the CME-3 event, there is no clear source region observation. The tilt angle and half angle are fixed to -10^o and 11^o, respectively, to get the best fitting of the CME shapes observed by both the STA and STB. The GCS flux rope can fit the CME fairly well as shown in the Figure 12. Table 4 lists the parameters of all the 15 data points of the event.

Figure 13(a) shows the height-time plot of the CME, and suggests a slight acceleration during the propagation. The average speed of the CME is 285.8 km$\cdot s^{-1}$, and the average acceleration is 4 m$\cdot s^{-2}$. The variations of the Stonyhurst longitude and latitude of the CME are shown in Figure 13(b) and 13(c), respectively. Neither the Stonyhurst longitude nor the latitude shows a significant change. There is no more than 3^o variation of the longitude. The latitude just changed slightly from 22.6^o to 19.6^o in the COR1 FOV and did not vary in the COR2 FOV. Moreover, its deflection rate is no more than $3^o/R_s$ as shown in Figure 13(d). Thus, this CME could be taken as the event without an obvious deflection during its propagation.

The comparison between the deflections and the magnetic field energy density distributions of every

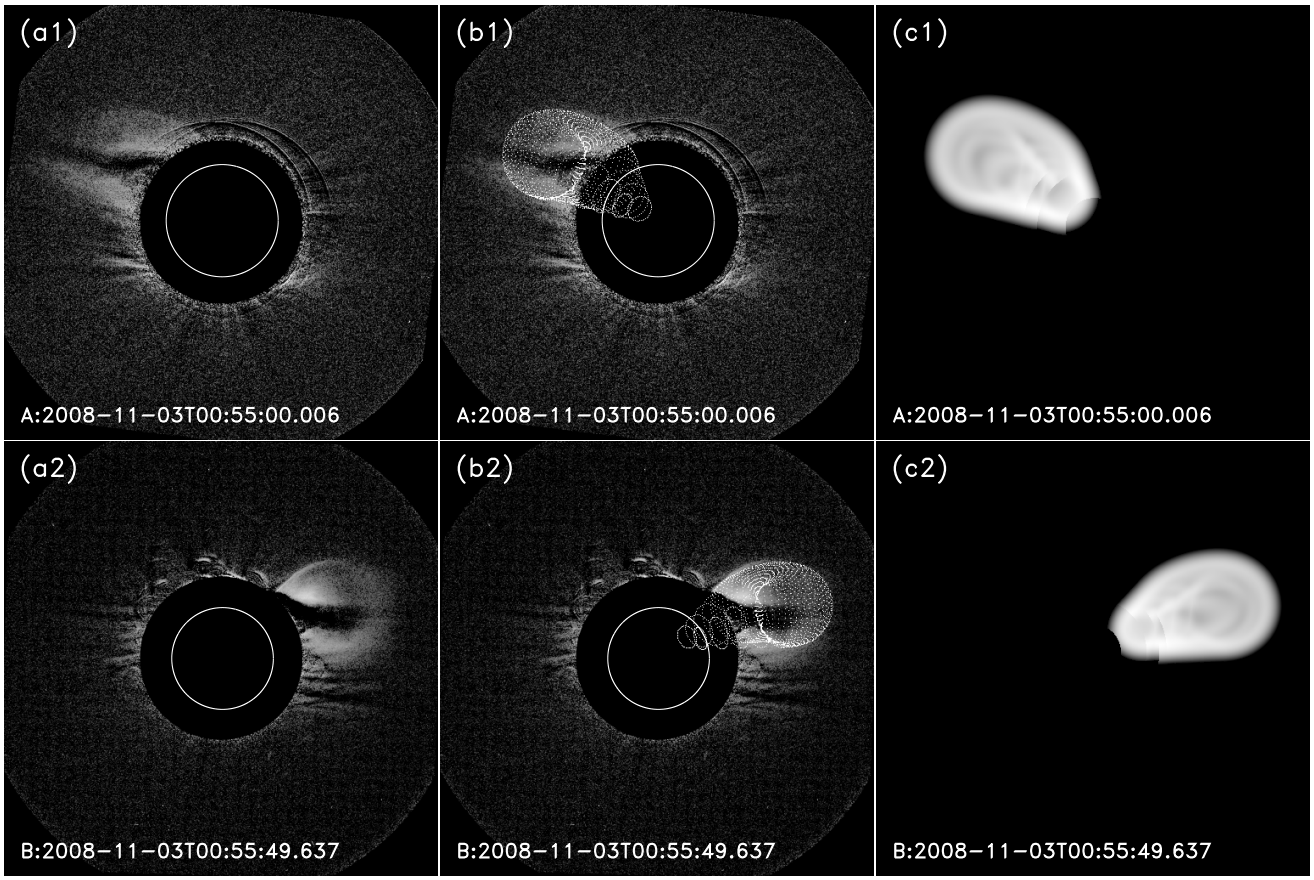

Figure 12: The fitting example of the CME-4. From (a) to (c): The original CME images, the modeled wireframe images which overlays on the CME images and the relative brightness derived from the GCS model. The upper and bottom panels present the results based on the STA and the STB, respectively.

data points are presented in Figure 14. The synoptic chart of the 2076 Carrington rotation which begins at 23:42 UT 2008 October 23 and ends at 07:00 UT 2008 November 20 is adopted as the bottom boundary of the CSSS model. From the figure, it can be seen that the minus gradient direction of the magnetic energy density is toward to the nearby HCS. The CME direction changes almost do not align with the minus gradient directions. Compared to the previous three events, both the deflection rate and the minus gradient for this event are quite small. Thus the large deviation between the two directions should not be an inconsistency.

4 Preliminary statistical results of CME deflections

In the above analysis, we present four events which manifest different deflection properties during their propagation in the corona. The first two events: the 2008 December 12 event (CME-1) and the 2008 April 9 event (CME-2), which appeared apart from the heliospheric current sheet at the early stage, deflected basically along the minus gradient direction of the magnetic energy density. Both of them get closer to the HCS which generally locates at the region with the lowest magnetic energy density. The 2007 November 16 event (CME-3), which initially originated near the HCS, manifested a deflection along the HCS that is in both longitudinal and latitudinal directions. The 2008 November 3 event (CME-4) did not exhibit an evident deflection, and accordingly the minus gradient of magnetic energy density was also very small.

Besides the above four events, another six events which have clear observations in the FOVs of the COR1 and the COR2 during the period from November 2007 to the end of 2008 have also been studied. The main parameters of all the ten events are listed in Table 5. For each event we give the parameters at the first and the last valid time and list them in two rows.

It could be found from Table 5 that there are

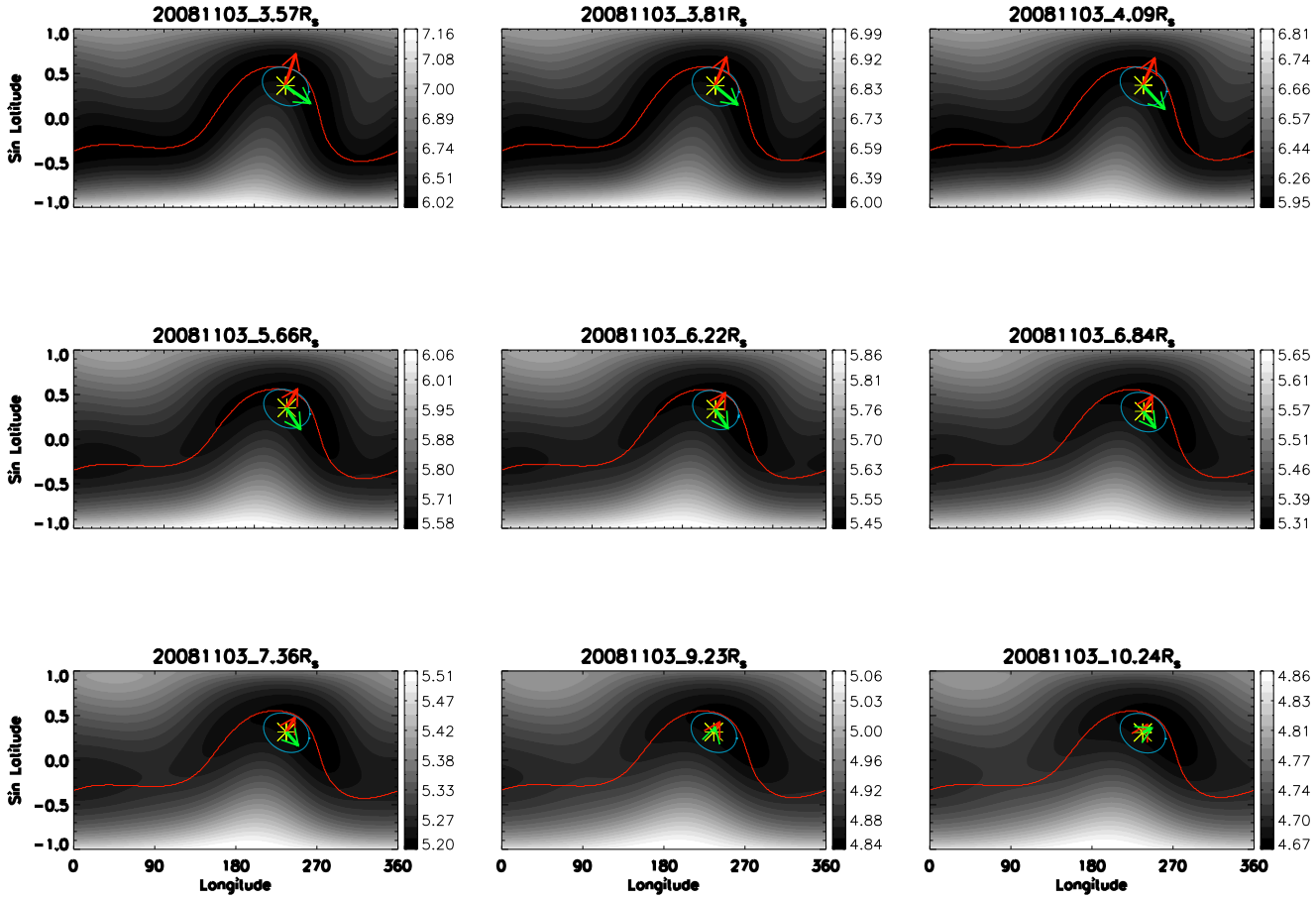

Figure 14: Same as the Figure 4, but for the 2008 November 3 event.

two events which erupted on 2008 January 22 and 2008 November 3 (CME-4) did not deflect obviously. The other events all manifested a deflection during the propagation. Especially the events erupting on 2007 November 16 (CME-3) and 2008 November 13 deflected in both longitudinal and latitudinal directions. Similar to CME-3, the 2008 November 13 CME also deflected along the HCS.

For all the events, we have a total of 118 data points of deflection, minus gradient, and the corresponding information such as height, the instantaneous velocity, etc. Figure 15(a) shows the distribution of the angle between the directions of the deflection and the minus gradient. It can be read from the histogram that the fraction of event decreases from small angle (agreement between the direction of the gradient of magnetic energy density and the deflection) to large angle (disagreement). The bin of the angle $\leq 15^{o}$ has the most data points, almost half the data points have the angle $\leq 45^{o}$, and as much as 80% data points have the angle $\leq 90^{o}$. The angle $\leq 90^{o}$ means that the deflections are marginally consistent with the minus gradients, and the angle $\leq 45^{o}$ indicates a good consistency. Figure 15(b) presents the probability of the angle $\leq 90^{o}$ (diamond) and $\leq 45^{o}$ (asterisk), respectively, as a function of the height of the CME leading edge. At any height, there are at least 80% of data points with the angle $\leq 90^{o}$, and at least 45% of data points with the angle $\leq 45^{o}$. Particularly, the probabilities are higher within about 6 R_s, which suggests that the deflections and the minus gradients have a better consistency in the inner corona. Figure 15(c) has the same meaning as the Figure 15(b), but presents the probability versus the strength of the magnetic energy density gradient. It is clearly shown that the deflections and the minus gradients have a better consistency when the gradient is stronger. When the gradient is larger than $5 \times 10^{-7} J \cdot km^{-4}$, the two directions are marginally consistent, while the gradient is larger than $5 \times 10^{-3} J \cdot km^{-4}$, they are strongly consistent.

Date	Time/UT	$\phi_c/^o$	$\phi_s/^o$	$\theta/^o$	h_f/R_s	κ	$\gamma/^o$	$\alpha/^o$	$\triangle\alpha^o$	$V/km/s$	N
16-Nov-07	09:35	303.1	101.1	-22.2	3.0	0.25	-24.6	8.4	24.0	255	11
	15:22	322.4	123.6	-13.6	12.0	0.27					
04-Dec-07	06:05	34.3	67.6	14.2	3.3	0.14	-56.5	10.1	11.9	182	19
	16:52	34.2	73.4	3.9	13.8	0.21					
22-Jan-08	22:45	226.7	194.6	-23.8	3.7	0.27	-21.8	10.1	1.9	296	16
	$06:22^n$	223.9	196.0	-25.2	16.4	0.36					
23-Feb-08	17:05	224.1	250.2	21.5	3.5	0.21	25.7	11.7	6.0	174	25
	$06:22^n$	211.2	244.6	19.2	15.5	0.24					
25-Mar-08	19:05	194.2	270.0	-12.8	2.5	0.25	35.2	12.6	8.5	1092	4
	20:52	201.7	278.4	-12.3	12.7	0.30					
05-Apr-08	16:15	260.8	120.1	1.3	3.3	0.17	-64.8	9.8	8.1	982	5
	18:22	251.9	112.3	3.8	14.0	0.25					
09-Apr-08	10:45	187.6	96.6	-21.9	2.3	0.22	8.4	10.6	16.6	476	9
	14:52	201.6	112.9	-18.5	12.7	0.22					
03-Nov-08	00:05	235.5	7.6	22.6	3.2	0.23	-10.1	11.2	4.5	286	15
	06:52	234.6	10.4	19.0	13.1	0.23					
13-Nov-08	13:05	288.8	199.9	-22.3	3.0	0.24	-30.2	11.2	13.4	256	24
	21:22	275.5	191.1	-12.1	16.4	0.27					
12-Dec-08	05:35	72.8	2.0	30.7	2.5	0.22	-15.1	14.0	22.1	276	24
	14:52	74.3	8.7	9.6	17.4	0.29					

Table 5: The fitted free parameters of all the CME events. For each event, the parameters at the first and last valid times are given in two rows. Column "Date" gives the date when the CME occurred. The second column lists the time when the CME observed and the superscript 'n' means the time of the next day. The next seven columns give the model parameters: the Carrington longitude 'ϕ_c', the Stonyhurst longitude 'ϕ_s', latitude 'θ', height 'h_f', ratio 'κ', tilt angle 'γ', and half angle 'α'. The 10th column means the solid angle between the first and the last data point. The next two columns give the average speed of the event and the total number of data points.

A further quantitative analysis about the deflection rate is shown in the Figure 16. The data points with the angle between the directions of the deflection and the minus gradient larger than 90^o are defined as 'bad points' and indicated by the red diamonds. Figure 16(a) shows the deflection rate as a function of the height. It is found that the deflection rate of the CMEs decreases quickly with increasing height. The CMEs generally have large deflection rate within about 4 R_s, and in the outer corona, the deflection rate approaches to zero. None of the bad points is beyond the deflection rate of $3^o/R_s$.

The correlation between the deflection rate and the strength of the magnetic energy density gradient is shown in Figure 16(b). The gray scale indicates the instantaneous radial speed of CMEs. The darker symbol stands for the larger speed. It is found that all the 'bad points' (shown in red diamonds) appeared in the area with the minus gradient lower than $5 \times 10^{-3} J \cdot km^{-4}$ and the deflection rate within $3^o/R_s$. In such a region, any errors in our calculation may become relatively significant. Thus, as we have stated before, these 'bad points' cannot be treated as an inconsistency. Without these bad points, there is an evident positive correlation between the deflection rate and the gradient strength. The correlation coefficient is about 0.85. It suggests that a stronger gradient cause a larger deflection rate. Considering the deflection rate is not significant when the minus gradient is lower than 10-4 J.km-4, we also show the correlation between the deflection rate and the gradient strength for the data points with the gradient strength larger than $10^{-4} J \cdot km^{-4}$, which is represented by the solid line in the Figure 16(b). It still shows a positive correlation, though the correlation coefficient decreases to 0.58.

The relative low correlation coefficient is mainly due to the significant scattering of the data points at the right-upper corner. We notice that there are three data points at strong gradients but having a relatively small deflection rate (marked by '$\triangle$'), and other three data points with a large deflection but at relatively weak gradients (marked by '$\square$'). The two sets of data points obviously opposite to the overall correlation we obtained, and may imply that there should be other factors influencing the

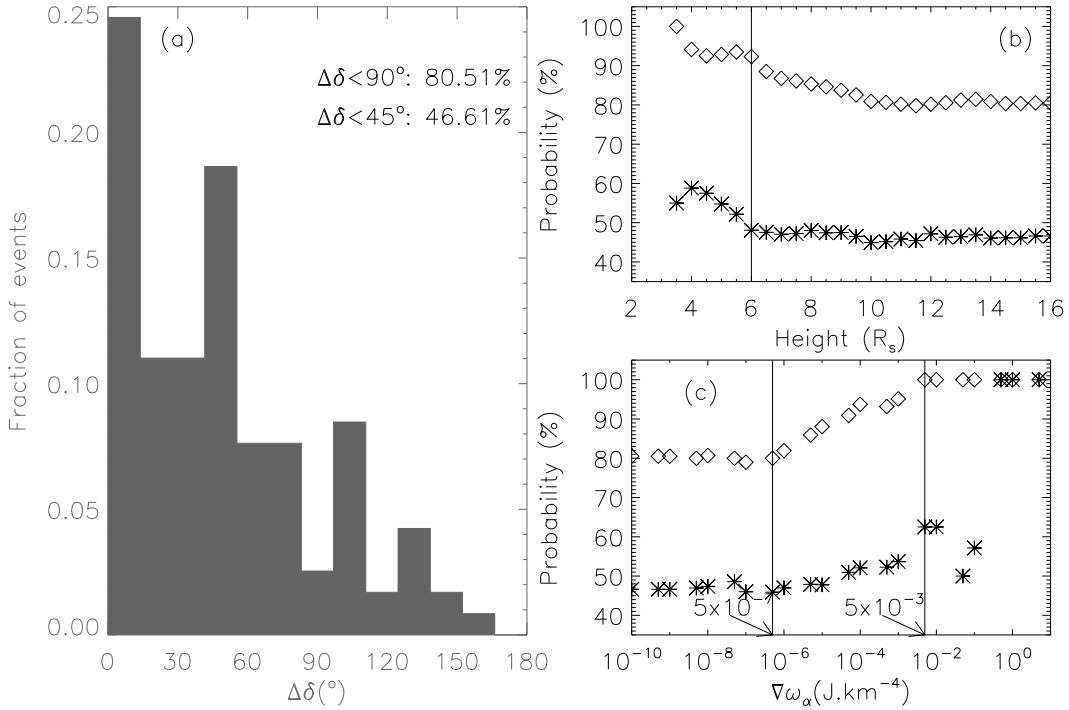

Figure 15: The statistical analysis of the angle between the deflection and the minus gradient. (a) The distribution of the angle. (b) The probabilities of the angle $\leq 90^{o}$ (diamond) and $\leq 45^{o}$ (asterisk) as a function of the height. (c) Same as the figure (b), but presents the probabilities as a function of the strength of the magnetic energy density gradient.

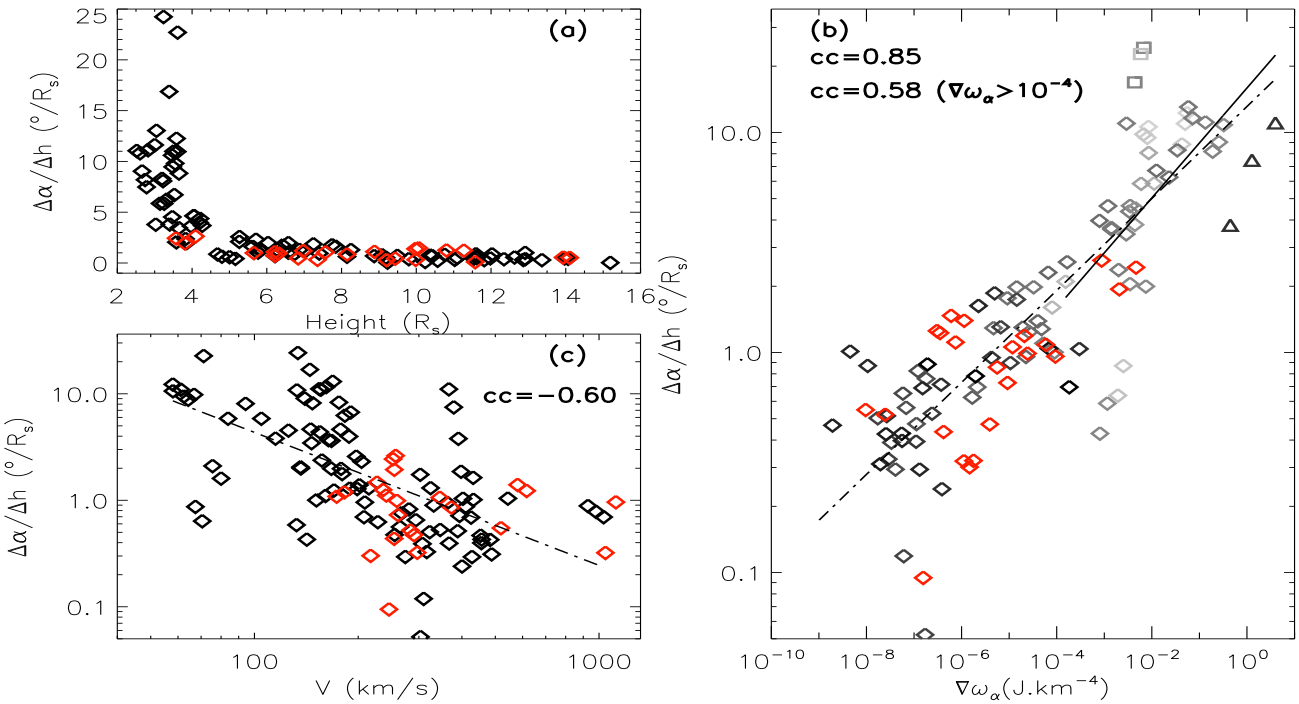

Figure 16: The quantitative analysis about the deflection rate. The red diamonds mark the 'bad' points, at which the deflection direction is opposite to the minus gradient. (a) Scattering plot of the deflection rate versus the height. (b) Scattering plot of the deflection rate versus the strength of the gradient. The grayscale of the symbols indicates the instantaneous radial speed of CMEs. The darker color stands for the larger speed. (c) The scattering plot of the deflection rate versus the instantaneous radial speed.

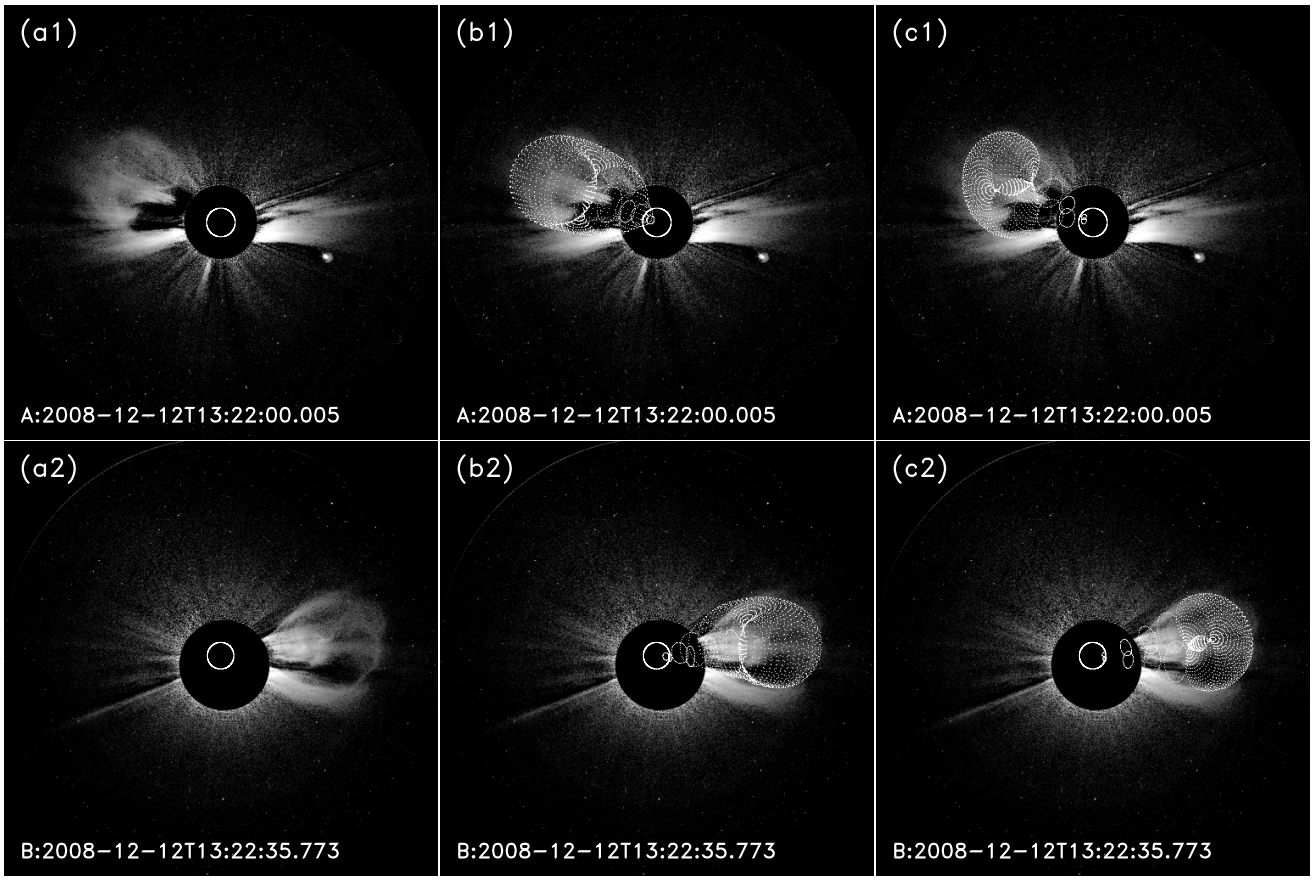

Figure 17: The fitting example of the CME-1 of the GCS model with the tilt angle of -15^{o} and -84^{o}. From (a) to (c): The original CME images, the modeled wireframe images with the tilt angle of -15^{o} and -84^{o}. The upper and bottom panels present the results based on the STA and the STB, respectively.

deflection rate of CMEs.

A possible factor is the CME radial speed. By comparing the deflection rate of these data points with the CME radial speed (derived from height-time plot, see Fig. 3(a) for example), we found that the speeds of the data points '△' are bigger than those of the data points '□'. For all the other data points, Figure 16(c) shows the deflection rate as a function of the CME radial speed. A weak anti-correlation could be found between the deflection rate and the speed. The data points with a higher speed generally experience a slower deflection, i.e., the faster a CME moves outward, the smaller is the deflection rate.

Besides, the CME mass should be another important factor. Mass characterizes the inertia of a CME. Thus, the heavier a CME is, the smaller should be the deflection rate. However, there are only 4 events having available mass in the CDAW CME catalog (http://cdaw.gsfc.nasa.gov/CME_list/). The event number is too small to derive a reliable result. Moreover, considering that there are significant errors in the mass determination [Colaninno and Vourlidas, 2009; Lugaz et al., 2005; Vourlidas et al., 2000; Wang et al., 2011], the effect of CME mass on the deflection is not analyzed in this paper.

5 Summary and discussion

In this paper, the deflections of the ten CMEs which occurred from November 2007 to the end of 2008 were studied. With the aid of the GCS model, eight of these CMEs are found to be deflected during its propagation in the corona. The distribution of the coronal magnetic field extrapolated from the SOHO/MDI magnetic synoptic charts suggests that the CMEs tend to deflect to the region with lower magnetic energy density. It confirms the result of Shen et al. [2011].

The further quantitative analysis here reveals that the deflections and the minus gradients have a better consistency in the lower corona or in the re-

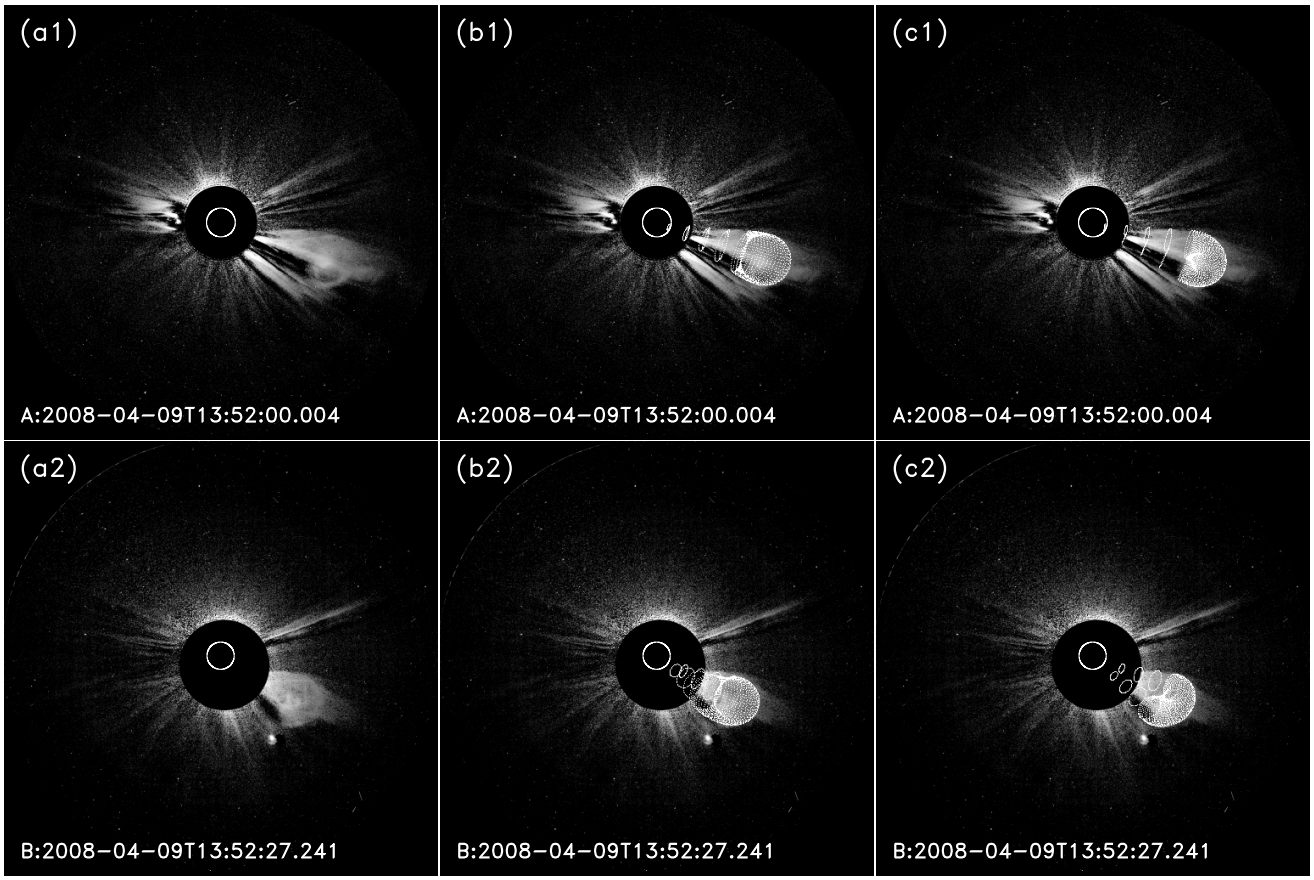

Figure 19: The fitting example of CME-2 with the GCS model of different tilt angle. From (a) to (c): The original CME images, the modeled wireframe images with the tilt angle of 8° and −39°. The upper and bottom panels present the results based on the STA and the STB, respectively.

gion with a strong gradient of the magnetic energy density. The comparison of the deflection rate to the CME height and the speed suggests that CMEs have higher deflection rates in the inner corona, generally below 4 R_s. There is a positive correlation between the CME deflection rate and the strength of the magnetic energy density gradient. A stronger gradient may cause a larger deflection rate. Meanwhile, the CME speed has a negative effect on the deflection rate. A faster event tends to have a slower deflection. It is due to the gradient force of the magnetic energy density acting on the fast event lasted much shorter than that acting on the slow CME.

The fixed tilt angle implies the hypothesis that the CME did not rotate during the period of interest. We realized that this hypothesis may not be true. But it does not affect our result, because, even if we adjust the value of the tilt angle, the key parameters we cared about, including the longitude, latitude and height, do not significantly changed as long as the GCS flux rope can fit the observed CME well. Listed below are two examples illustrating this issue.

In our study, the tilt angle of the CME-1 was fitted to −15°. When we adjust the tilt angle, it is found that the GCS flux rope with the tilt angle of −84° also fits the observations well. Figure 17 compares the GCS model result between the two tilt angles, and Table 6 listed the parameters for the comparison with Table 1.

At the tilt angle of −15° the GCS flux rope is in axial-view, while at the tilt angle of −84° the GCS flux rope is in side-view. Although the tilt angles are very different, the key parameters don't have significant differences. The maximal differences of the height, longitude and latitude between the two cases are about 0.2 R_s, 4° and 2°, respectively. The variations of the three parameters are also shown by the asterisks and diamonds in Figure 18. It can be seen that the two symbols are almost overlapped.

This event was studied by Liu et al. [2010b], in which the tilt angle was chosen as −53°. By

Time/UT	ϕ_c/°	ϕ_s/°	θ/°	h_f/R_s	κ
		COR1			
05:35	72.0	1.2	28.8	2.54	0.16
05:45	75.3	4.6	28.2	2.56	0.16
05:55	74.0	3.4	26.9	2.67	0.16
06:05	74.6	4.0	26.8	2.73	0.16
06:15	73.7	3.3	26.7	2.76	0.17
06:25	74.3	3.9	26.0	2.81	0.17
06:35	72.8	2.6	25.7	2.85	0.17
06:45	73.1	2.9	24.4	3.11	0.17
06:55	74.3	4.3	24.3	3.24	0.17
07:05	74.6	4.6	23.4	3.37	0.17
07:15	74.5	4.6	22.6	3.63	0.17
07:25	74.5	4.7	21.6	3.85	0.18
07:35	74.4	4.7	20.2	4.02	0.18
		COR2			
09:52	73.4	4.9	12.3	6.99	0.20
10:22	75.9	7.7	12.4	8.03	0.20
10:52	72.8	4.9	11.8	9.04	0.20
11:22	76.0	8.4	11.3	9.97	0.20
11:52	74.0	6.6	10.4	11.33	0.20
12:22	74.3	7.2	9.5	11.89	0.20
12:52	74.5	7.7	9.4	13.28	0.20
13:22	75.5	9.0	9.4	14.03	0.20
13:52	74.9	8.7	8.3	15.13	0.20
14:22	75.0	9.0	8.4	16.28	0.20
14:52	73.2	7.5	8.2	17.59	0.20

Table 6: The fitted free parameters of the 2008 December 12 CME derived by the GCS model with the tilt angle of −84° and the half angle of 8°

Time/UT	ϕ_c/°	ϕ_s/°	θ/°	h_f/R_s	κ
		COR1			
10:45	186.7	95.8	-20.8	2.36	0.11
10:55	190.7	99.8	-20.6	2.56	0.11
11:05	191.2	100.4	-20.1	2.79	0.11
11:15	191.7	101.1	-20.2	3.04	0.11
11:25	193.2	102.6	-19.4	3.32	0.11
		COR2			
13:22	197.5	108.0	-19.7	8.57	0.14
13:52	197.1	108.0	-19.5	9.84	0.14
14:22	199.8	111.8	-20.0	11.27	0.14
14:52	199.8	111.1	-20.5	12.73	0.14

Table 7: The fitted free parameters of the 2008 April 9 CME derived by the GCS model with the tilt angle of −39° and the half angle of 10°

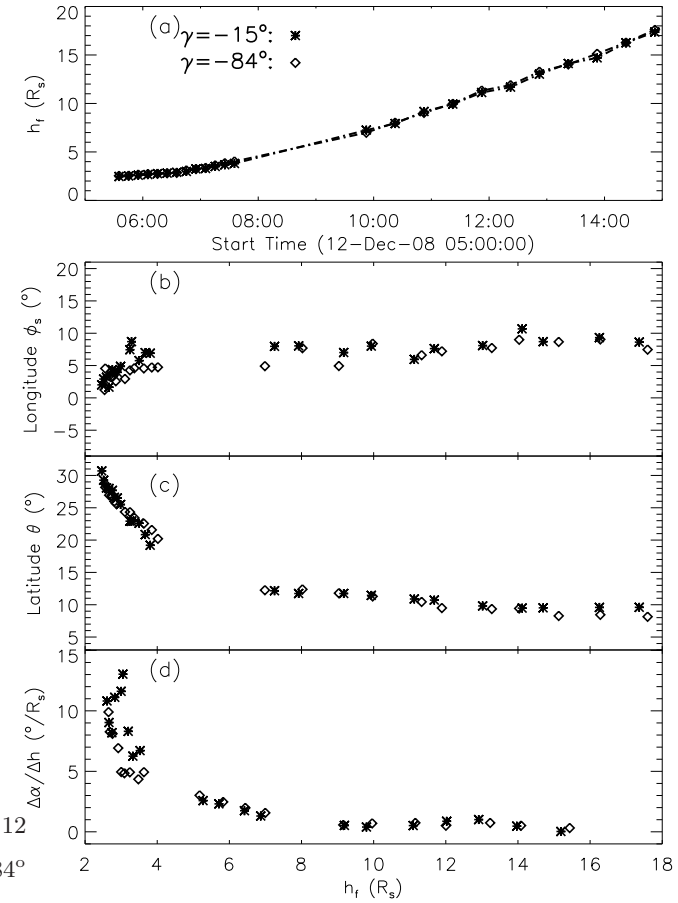

Figure 18: The comparison between the kinetic evolutions of the CME-1 event which derived by the GCS model with two different tilt angles. The asterisks and the diamonds present the GCS model with the tilt angle of −15° and −84°, respectively. Panels (a) to (d) show the height-time, longitude-height, latitude-height, and deflection rate-height curves, respectively.

comparing our results with the parameters which derived by the GCS model with the tilt angle of −53° for the data point recorded at 12:52 UT given in the paper of Liu et al. [2010b], it is found that the differences in longitude and latitude are both 2° only.

Similar to the CME-1 event, we find that the GCS flux rope with the tilt angle of −39° also fits the observed shape of CME-2. The fitting results of the GCS model with the different tilt angle are presented in Figure 19 and listed in Table 7. Although the tilt angles are different, the key parameters don't have significant differences. The maximal differences of the height, longitude and latitude between the two different tilt angles are about 0.1 Rs, 2° and 2°, respectively. Also evolutions of the height, longitude and latitude of the CME under the two different conditions are quite similar, as shown by the asterisks and diamonds in Figure 20.

In addition, six of our ten events were also listed in Table 1 of the paper by Thernisien et al. [2009]. By comparing our Table 5 with that table, we find that the difference between the longitudes is mostly within 4° and four of the six events are just 2°, and the difference between the latitudes is less than 1° expected for one event, which is about 3°. It is no-

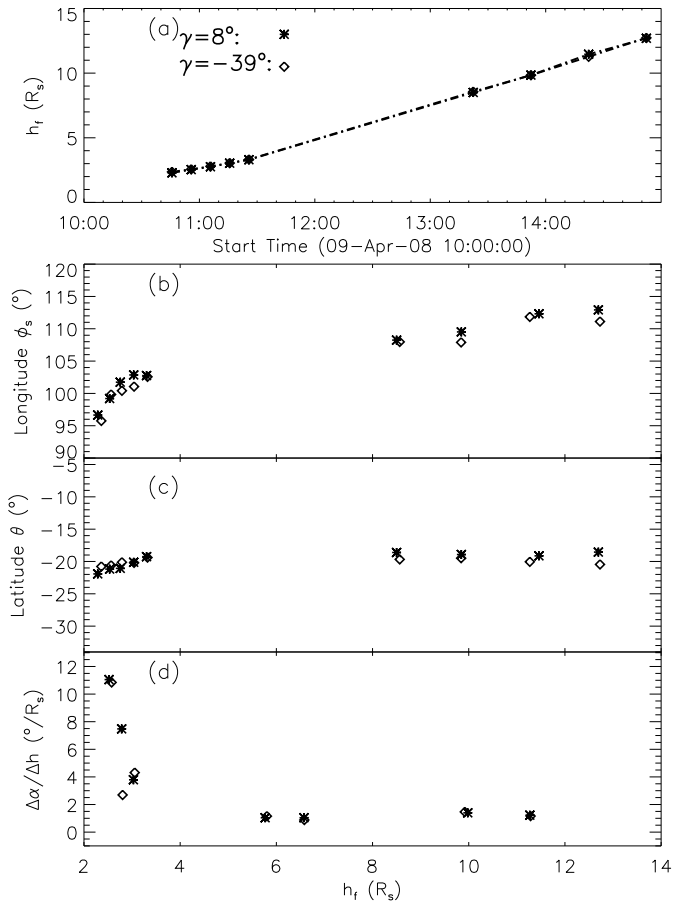

Figure 20: The comparison between the kinetic evolutions of the CME-2 event which derived by the GCS model with the two different tilt angles. The asterisks and diamonds present the GCS model with the tilt angle of 8° and −39°, respectively. Panels (a) to (d) show the height-time, longitude-height, latitude-height, and deflection rate-height curves, respectively.

ticed the longitudinal difference for the data point recorded at 17:52 UT of the 2008 April 5 event is about 14°. By fitting the CME images with the parameters given by Thernisien et al. [2009], we find that the difference is caused by the different front edge selection. Even if we adopted the CME front edge selected by Thernisien et al. [2009], and performed the same analysis, it can be found that the CME would manifest the same deflection behavior.

In summary, the CME deflection is mainly controlled by the gradient of the coronal magnetic field based on the statistical study. The results confirm that the theoretical method proposed by the Shen et al. [2011] is able to quantitatively describe the CME deflections. Moreover, we believe that the method can be developed into a promising model, magnetic energy density gradient (MEDG) model, of predicting the CME deflection in the corona, though the basic idea of it is very simple. In this model, the gradient of the magnetic energy density is treated as a major cause of the CME deflection. Actually, the polarity of the background magnetic field may also have effect on the deflections of CMEs [Chané et al., 2005; Isenberg and Forbes, 2007]. Besides, it should be noted that the gradient of the magnetic energy density decrease quickly with increasing height. When a CME propagates outward, the gradient of the background magnetic field may become weak rapidly. Such weak gradient would not be sufficient to make a CME deflected obviously especially during the CME propagates in the interplanetary space. This implies that there should be another mechanism to cause the CME deflection in the interplanetary space, which had been reported by Poomvises et al. [2010] and Lugaz et al. [2010]. A possible candidate mechanism is the CME's interaction with the background solar wind as proposed by Wang et al. [2004, 2006].

Acknowledgments. We acknowledge the use of the data from STEREO/SECCHI and SOHO/MDI. We also acknowledge the use of the GCS model that developed by A. Thernisien. We are grateful to the anonymous referee for his/her kindly and constructive comments. This work is supported by grants from 973 key projects 2011CB811403, NSFC 40874075, 40904046, FANEDD 200530, CAS KZCX2-YW-QN511, 100-Talent program of CAS, and the fundamental research funds for the central universities.

References

Brueckner, G. E., R. A. Howard & M. J. Koomen, et al., The Large Angle Spectroscopic Coronagraph (LASCO), Sol. Phys., 162 (1-2), 357-402, 1995.

Byrne, J. P., S. A. Maloney, R. T. McAteer, J. M. Refojo & P. T. Gallagher, Propagation of an Earth-directed coronal mass ejection in three dimensions, Nature Communications, 1, 74, 2010.

Chané, E., C. Jacobs, B. van der Holst, S. Poedts & D. Kimpe, On the effect of the initial magnetic polarity and of the background wind on the evolution of CME shocks, Astronomy & Astrophysics, 432, 331C339, 2005.

Colaninno, R. C. & A. Vourlidas, First Determination of the True Mass of Coronal Mass Ejections: A Novel Approach to Using the Two STEREO Viewpoints, Astrophys. J., 698, 852-858, 2009.

Cremades, H. & V. Bothmer, On the three-dimensional configuration of coronal mass ejections, Astronomy & Astrophysics, 422, 307C322, 2004.

Cremades, H., V. Bothmer & D. Tripathi, Properties of structured coronal mass ejections in solar cycle 23, Adv. Space Res., 38, 461, 2006

Davis, C. J., J. A. Davies, M. Lockwood, A. P. Rouillard, C. J. Eyles, & R. A. Harrison, Stereoscopic imaging of an Earth-impacting solar coronal mass ejection: A major milestone for the STEREO mission, Geophys. Res. Lett., 36, L08102, 2009.

Gopalswamy, N., S. Yashiro, S. Krucker, G. Stenborg, & R. A. Howard, Intensity variation of large solar energetic particle events associated with coronal mass ejections, J. Geophys. Res., 109, A12105, 2004

Gopalswamy, N., S. Yashiro, G. Michalek, H. Xie, R. P. Lepping, & R. A. Howard, Solar source of the largest geomagnetic storm of cycle 23, Geophys. Res. Lett., 32, L12S09, 2005.

Gopalswamy, N., P. Mäkelä, H. Xie, S. Akiyama, & S. Yashiro, CME interactions with coronal holes and their interplanetary consequences, J. Geophys. Res., 114, A00A22, 2009.

Howard, R. A., J. D. Moses & A. Vourlidas, et al., Sun Earth Connection Coronal and Heliospheric Investigation (SECCHI), Space Sci Rev, 136, 67C115, 2008.

Isenberg, P. A. & T. G. Forbes, A Three-dimensional Line-tied Magnetic Field Model for Solar Eruptions, Astrophys. J., 670, 1453-1466, 2007.

Kaiser, M. L., T. A. Kucera, J. M. Davila, O. C. St. Cyr, M. Guhathakurta & E. Christian, The STEREO Mission: An Introduction, Space Sci Rev, 136, 5C16, 2008.

Kilpua, E. K. J., J. Pomoell, & A. Vourlidas, et al., STEREO observations of interplanetary coronal mass ejections and prominence deflection during solar minimum period, Annales Geophysicae, 27, 4491, 2009.

Liu, Y., J. A. Davies, J. G. Luhmann, A. Vourlidas, S. D. Bale & R. P. Lin, Geometric triangulation of imaging observations to track Coronal Mass Ejections continuously out to 1 AU, Astrophys. J., 710, 82-87, 2010a.

Liu, Y., A. Thernisien & J. G. Luhmann, et al., Reconstructing Coronal Mass Ejections with Coordinated Imaging and in Situ Observations: Global Structure, Kinematics, and Implications for Space Weather Forecasting, Astrophys. J., 722, Issue 2, pp. 1762-1777, 2010b.

Lugaz, N., W. B. IV Manchester & T. I. Gombosi, The Evolution of Coronal Mass Ejection Density Structures, Astrophys. J., 627, 1019-1030, 2005.

Lugaz, N., J. N. Hernandez-Charpak, I. I. Roussev, C. J. Davis, A. Vourlidas, & J. A. Davies, Determining the azimuthal properties of coronal mass ejections from multi-spacecraft remote-sensing observations with STEREO SECCHI, Astrophys. J., 715, 493-499, 2010.

Lynch, B. J., S. K. Antiochos, Y. Li, J. G. Luhmann, & C. R. DeVore, Rotation of Coronal Mass Ejections during Eruption, Astrophys. J., 697, Issue 2, pp. 1918-1927, 2009.

MacQueen, R. M., A. J. Hundhausen, & C. W. Conover, The propagation of Coronal Mass Ejection transients, J.Geophys. Res., 91(A1), 31-38, 1986.

Möstl, C., C. Miklenic & C. J. Farrugia, et al., Two-spacecraft reconstruction of a magnetic cloud and comparison to its solar source, Annales Geophysicae, 26, 3139-3152, 2008.

Ness, N. F. & J. M. Wilcox, Solar origin of the interplanetary magnetic field, Phys. Rev. Lett., 13, 461-464, 1964.

Poomvises W., J. Zhang & O. Olmedo, Coronal Mass Ejection propagation and expansion in three-dimensional space in the Heliosphere based on STEREO/SECCHI observations. Astrophys. J., 717, L159CL163, 2010.

Shen, C., Y. Wang, B. Gui, P. Ye & S. Wang, Kinematic evolution of a slow CME in corona viewed by STEREO-B on 8 October 2007, Solar Phys., 269, 389C400, 2011.

Shen, C., Y. Wang, P. Ye, X. P. Zhao, B. Gui & S. Wang, Strength of Coronal Mass Ejection-driven shocks near the Sun, and its importance in prediction of Solar Energetic Particle events, Astrophys. J., 670, 849, 2007.

Shiota, D., K. Kusano, T. Miyoshi & K. Shibata, Magnetohydrodynamic modeling for a formation process of Coronal Mass Ejections: interaction between an ejecting flux rope and an ambient field, Astrophys. J., 718, 1305C1314, 2010.

Thernisien, A.F.R., R. A. Howard & A. Vourlidas, Modeling of flux rope coronal mass ejections, Astrophys. J., 652, 763C773, 2006.

Thernisien, A., A. Vourlidas, & R. A. Howard, Forward Modeling of Coronal Mass Ejections using STEREO/SECCHI data, Solar Phys., 256, 111C130, 2009.

Thompson, W. T., Coordinate systems for solar image data. Astronomy & Astrophysics, 449(2): 791 803, 2006.

Török, T. & B. Kliem, The evolution of twisting coronal magnetic flux tubes, Astronomy & Astrophysics, 406, 1043-1059, 2003.

Vourlidas, A., P. Subramanian, K. P. Dere & R. A. Howard, Large-Angle Spectrometric Coronagraph Measurements of the Energetics of Coronal Mass Ejections, Astrophys. J., 534, 456, 2000.

Wang, Y., C. Chen, B. Gui, C. Shen, P. Ye & S. Wang, Statistical Study of CME Source Locations: I. Understanding CMEs Viewed in Coronagraphs, J. Geophys. Res., in press, doi: 10.1029/2010JA016101, 2011.

Wang, Y., C. Shen, S. Wang & P. Ye, Deflection of Corona Mass ejection in the interplanetary medium, Solar Phys., 222, 329C343, 2004.

Wang, Y., X. Xue, C. Shen, P. Ye, S. Wang, & J. Zhang. Impact of the major coronal mass ejections on geo-space during September 7 C 13, 2005. Astrophys. J., 646, 625C633, 2006.

Wang, Y., P. Ye, S. Wang, G. Zhou & J. Wang, A statistical study on the geoeffectiveness of Earth-directed coronal mass ejections from March 1997 to December 2000, J. Geophys. Res., 107 (A11), 1340, 2002.

Wang, Y. & J. Zhang, A Comparative Study between Eruptive X-class Flares Associated with Coronal Mass Ejections and Confined X-class Flares, Astrophys. J., 665, 1428, 2007.

Wang, Y., G. Zhou, P. Ye, S. Wang & J. Wang, A study on the orientation of interplanetary magnetic clouds and solar filaments, Astrophys. J., 651, 1245-1255, 2006.

Yurchyshyn, V., Q. Hu, R. P. Lepping, B. J. Lynch & J. Krall, Orientations of LASCO Halo CMEs and their connection to the flux rope structure of interplanetary CMEs, Advances in Space Research, 40, 1821-1826, 2007.

Yurchyshyn, V., V. Abramenko & D. Tripathi, Rotation of White-light Coronal Mass Ejection Structures as Inferred from LASCO Coronagraph, Astrophys. J., 705, 426-435, 2009.

Zhao, X. P., & J. T. Hoeksema, Prediction of the interplanetary magnetic field strength, J. Geophys. Res., 100, 19-33, 1995.